Dynamic focus-tracking MEMS scanning micromirror for an endoscopic, optical coherence tomography based imaging system

Matthew Strathman

A dissertation

submitted in partial fulfillment of the

requirements for the degree of

Doctor of Philosophy

University of Washington

2014

Reading Committee:

Prof. Lih Y. Lin, chair

R. Bruce Darling

Ruikang Wang

Program Authorized to Offer Degree:

Electrical Engineering

University of Washington

Abstract

Dynamic focus-tracking MEMS scanning micromirror for an endoscopic,
optical coherence tomography based imaging system

Matthew Strathman

Chair of the Supervisory Committee:
Prof. Lih Y. Lin
Dept. of Electrical Engineering

We demonstrate a 3-dimensional scanning micromirror device using micro-electromechanical systems (MEMS) technology to integrate 2-dimesional spatial scanning with dynamic focal control. The electrostatically actuated devices employ a biaxial gimbal structure, to allow 2-dimensional beam scanning, and a deformable mirror membrane, for focal tunability. The 800 micrometer diameter mirrors are designed to fit inside an imaging probe sufficiently compact for use in the working channel of a standard endoscope. Large optical scanning ranges of more than 20 degrees with low actuation voltages have been achieved with these micromirror devices. Additionally, tunable mirror curvature allows dynamic control of the focal length between infinite and 25 mm with less than 100 V. High mechanical resonant frequencies, of up to

500 Hz, allow faster repositioning of the optical beam and a higher frame rate for the imaging system.

These MEMS micromirror devices are used in an optical coherence tomography (OCT) imaging system. 2-dimensional, cross-sectional and spatial, images have been obtained using spectral-domain and time-domain OCT systems.

Table of Contents

List of Figures:

4.5	During release, undercutting of the gimbal occurs (a). Progression of the membrane release relies on chemical transport through etch vias on the surface of the mirror (b).
4.6	(A) A double side polished silicon wafer (B) The wafer is oxidized and silicon oxide pads are patterned (C) LPCVD is used to deposit a conformal silicon nitride (D) The backside is patterned and the silicon is thinned in the area of the mirrors (E) Electrical vias are etched through the nitride and the wafer is metallized (F) The gold, chrome and silicon nitride are etched before trenches are etched into the silicon (G) Hydrofluoric acid is used to etch the sacrificial silicon oxide layer. (H) KOH is used to etch a cavity in the silicon and finish the release of the device.
4.7	An optical microscope photograph (left) and a scanning electron micrograph (right) of a fabricated MEMS micromirror device.
4.8	Corner compensation allows protection of the convex corners of the silicon pillars during the progression of the KOH silicon etch. The layout design of the silicon nitride mask (left), an image a partially etched pillar with the undercut silicon nitride mask still visible (center) and the fully etched silicon pillar with an insulating oxide layer (right).
4.9	A finished silicon pillar with patterned aluminum electrodes. The ~400 µm tall pillar decreases the necessary actuation voltages by increasing the capacitance due to the mirror's proximity to the electrodes.
4.10	A Cross-section view of the 3-dimensional micromirror device with underlying aluminum electrodes.
4.11	Membrane curvature is controlled with an electric field beween the gold reflective layer and the underlying silicon. The membrane is flat with 0 volts applied (top) and curved when a non-zero voltage is applied (bottom).
4.12	Radius of curvature versus the applied voltage for the micromirror device with corresponding heat map showing the membrane surface height.
4.13	Heat maps corresponding to the height of the mirror surface (left) with 3-dimensional optical surface profiler images (right) for the mirror membrane with 0 volts (top) and 95 volts (middle) applied, and the membrane snapped down with 100 volts applied (bottom).
4.14	Cross-sectional image of the optical with color representing intensity. The beam passes through the focal point with a voltage from 70 V to 90 V.

Chapter 1: Introduction

Early diagnosis of diseases, particularly cancers, can often allow more successful treatment. While there are many diagnostic tools available to doctors, perhaps the most common is imaging. Imaging allows the doctor to visualize some aspect of the body, providing valuable insight and potentially aiding in diagnosis of health issues.

The aim of this research is the design and development of a 2-dimensional micromirror scanner with dynamic focal control based on micro-electromechanical systems (MEMS) technology. The target application for this micromirror is endoscopic imaging using optical coherence tomography. This type of imaging system can be used to generate high resolution, 3-dimensional images of tissue. Possibly the most common application of endoscopy is imaging of the gastrointestinal (GI) tract. Most current endoscopic imaging systems use a CCD imaging probe. This type of device is capable of very reliable digital imaging of tissue, however, several advantages can be realized in an OCT type imaging system. The main advantages of this type of system is the possibility of imaging sub surface tissue and ability to generate detailed 3-dimensional images.

Optical coherence tomography is an imaging method that has been used for over 20 years [1]. This technique employs a Michelson type interferometer to generate an interference signal from an optical signal from a scanned reference arm and from the sample. Chapter 2 of this dissertation will investigate previous use of endoscopy in medicine, from the first rigid endoscopes to modern, digital imaging systems. The operation and functionality of a time-domain OCT will be explained and then previous use of MEMS scanning and focal control devices for OCT will be discussed. In chapter 3, the physics of the micromirror operation and design are investigated. The equations governing the scanning of the micromirror under static and resonant actuation are derived. Then, the specific goals for the design of a MEMS micromirror scanner are discussed. The fabrication methods for these MEMS devices are explained in chapter 4, from the preliminary devices to the 3-dimensional scanning mirrors to the electrodes needed for electrostatic actuation. Additionally, the scanning and curvature control characteristics of fabricated devices are presented and discussed. Chapter 5 introduces devices designed for beam scanning in a spectral domain OCT system. Similar characterization measurements are presented for these devices. In chapter 6, the MEMS devices are integrated into time-domain and spectral-domain OCT systems. Successful spatial and depth imaging is demonstrated utilizing the fabricated devices. Chapter 7 will conclude this dissertation with a discussion of the outcome of this research and potential future work in this area.

Chapter 2: Background

Micro-electromechanical systems (MEMS) is a technology that utilizes processes developed by the semiconductor industry in order to realize complex mechanical systems on a very small scale. Feature sizes in MEMS devices are commonly in the single micrometer range [2]. The versatility of MEMS technology allows the miniaturization of very complex systems. The use of MEMS for sensing has yielded many commercial products such as accelerometers [3], gyroscopes [4], pressure sensors [5], etc. In the medical field the use of MEMS has allowed development of "lab on a chip" technologies, which allow chemical laboratory processes to be carried out by a very small self-contained device.

Another type of device that has been investigated by many researchers for many years is MEMS micromirrors. The interest in MEMS micromirrors is driven by the convenience of complex optical functionality, contained in a small package. Previous research in this area includes classic two-position devices, such as the TI DMD chip [6], but also more recent work on micromirror switches for use in optical communication systems [2], and the employment of MEMS mirrors for imaging [7]–[9].

This chapter investigates prior implementations of endoscopic imaging ranging from the first utilization of rigid endoscopes to the wide variety of modern designs. Additionally, optical coherence tomography, an interferometric imaging technique, will be introduced as a novel medical diagnostic tool. Finally, different approaches in MEMS technology for the integration of these two technologies, endoscopic imaging and OCT, will be discussed

2.1: Endoscopic imaging

Medical endoscopic imaging is the use of an endoscope to enable viewing or image capture of tissue inside the human body. This technique has been heavily utilized in the medical field as a tool for diagnosis. Endoscopic imaging has proven useful to nearly all fields of medicine, but perhaps the first and most common application is for imaging of the gastrointestinal tract. Early endoscopes generally used a rigid tube with small light generation devices, and imaging optics (fig. 2.1) [10]. These had the disadvantages of being uncomfortable and commonly harmful to the patient. The first truly flexible endoscopes, called fibroscopes, used a large fiber bundle to transmit the image out of the body [10]. In this system each optical fiber provides one pixel to the final image, therefore, the size of the optical fiber and the physical size constraint of the endoscope limited resolution and overall size of the images.

Fig. 2.1: The Nitze-Leiter gastroscope from 1879, an example of a rigid endosocope (left) and the flexible fibroscope (right). [10]

The most common modern endoscopes use very small CCD camera mounted on the endoscope tip [11]. This approach allows the transmission of high resolution images to a TV screen for convenient and consistent viewing. This type of device has been extensively utilized in medical diagnosis and laparoscopic surgeries in the last few decades. Recently, miniaturization of scanning optics and other microelectronic transducers has allowed the development of new endoscopic imaging probes. These new probes have the possibility of added functionality when compared to the standard CCD endoscope. For example, with a scanning imaging probe OCT can be used to generate 3-dimensional images that allow the subsurface layers of tissue to be visualized.

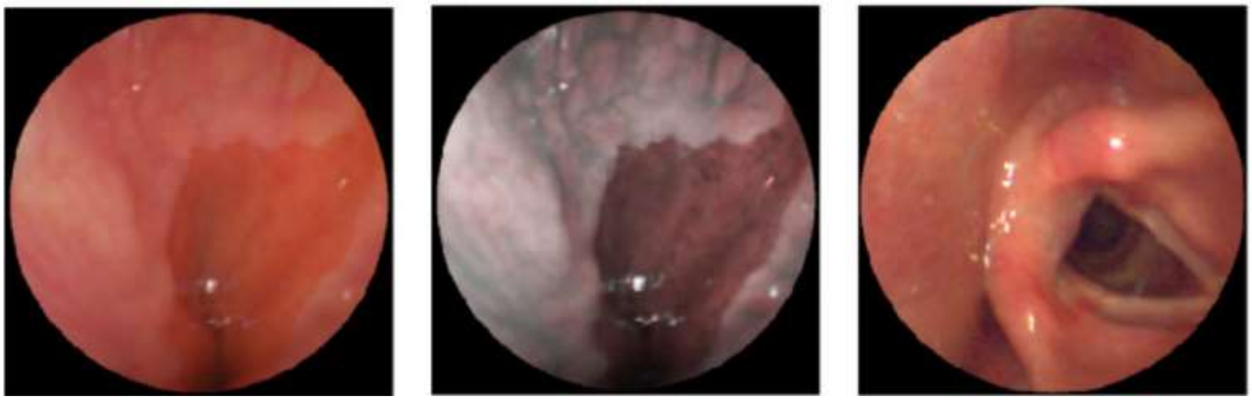

Fig. 2.2: Endoscopic images of the gastroesophageal junction of a human (left and center) and human vocal chords (right). [12]

2.2: Optical Coherence Tomography

OCT is a method of 3-dimensional image acquisition that has been proven very useful for imaging of tissue [1], [7]–[9], [12]–[23]. OCT uses interference generated between two optical paths to generate the imaging signal. There are 2 main classifications of OCT systems, time-domain and frequency-domain OCT. The difference in these two systems is the method of extracting the depth information. In a time-domain system the depth is controlled by altering the path length of the reference arm of the interferometer. In a spectral-domain system, however, the depth data is contained in the individual wavelengths and is extracted from the output optical signal with a spectrometer. The discussion here will be focused on time-domain OCT.

In a time domain OCT system the light is split between the sample and reference arms of a Michelson-type interferometer, by a beam splitter or a fiber coupler. A beam splitter is an optical component where a certain amount of incident light is reflected and the rest transmitted. A fiber coupler similarly splits the input light between two output optical fibers. The sample arm focuses the laser beam onto the sample and scans the beam over the desired image. The interference signal is generated when the lengths of both reference and signal arms are matched. This allows the imaging depth into the sample to be controlled by dynamically controlling the path length in the reference arm. The basic design of a time-domain OCT system is shown in fig. 2.3.

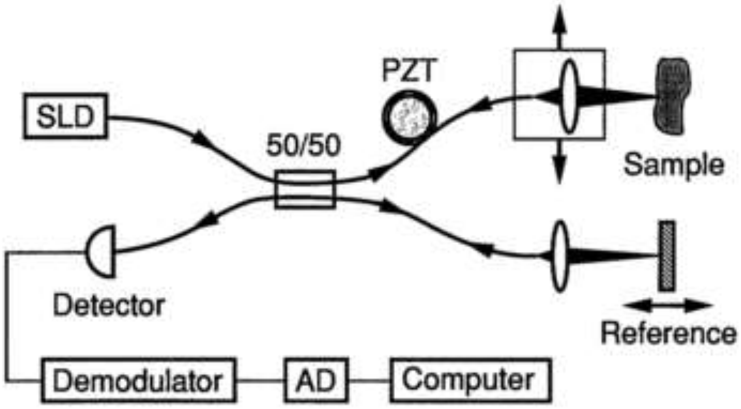

Fig. 2.3: Layout of the optical setup for a time-domain OCT system. [1]

3-dimensional imaging is accomplished through repetitious scanning in the vertical direction. While the beam is positioned at each of the lateral pixel locations, the path length of the reference arm is scanned. Each of these depth scans corresponds to one pixel in a lateral image.

In order to extract the intensity data from the signal the phase data in the signals must be analyzed. The electric field of the beams after the beam splitter is as follows:

$$E = E_0 e^{j2kz} \tag{Eq. 2.1}$$

After reflection off the reference mirror and the sample in the other arm, the electric fields of each arm can be expressed as:

$$E_r = E_0 r e^{j2kz_r} \tag{Eq. 2.2}$$

$$E_s = E_0 \sum_{n=0}^{N} r_{sn} e^{j2kz_{sn}} \tag{Eq. 2.3}$$

Where E_r and E_s are the electric fields of the signals after reflecting off the reference mirror and the sample respectively, r and r_{sn} are the reflectance of the reference mirror and sample respectively, z_r and z_{sn} are the phase added to each signal. As shown, the electric field of the sample arm is a summation of the reflections from all depths in the sample. After interfering the signals the electric field is the summation of the two signals above

$$E_i = E_0 r e^{j2kz_r} + E_0 \sum_{n=0}^{N} r_{sn} e^{j2kz_{sn}} \tag{Eq. 2.4}$$

A photodiode is used to capture this optical signal and convert it into an electrical signal that can be further processed. The photodiode measures the intensity of the incoming light, which is proportional to the magnitude of the electric field squared. Hence, the electrical signal contains a DC component that is caused by the reference signal and a Doppler shifted signal containing the pixel intensity data. This Doppler shift results from the continual change in path length of the reference arm. The shift frequency is dependent on the wavelength of the signal and the scanning rate of the reference arm.

$$f_D = \left(\frac{2 \cdot S}{\lambda}\right) \qquad \text{(Eq. 2.5)}$$

Where f_D is the Doppler frequency, S is the rate of path length change and λ is the wavelength of the signal. This Doppler shift allows this signal to be separated from the additional DC signal. The pixel intensity data corresponds to the magnitude of the signal at this frequency.

As discussed above, the optical signal from the sample arm of the OCT system contains reflectance data from various depths in the sample. The Doppler shifted signal, however, exists only in the interference signal. For interference to exist the path lengths must be matched within the coherence length of light source. This coherence length is a parameter that depends on the bandwidth of the optical source, its center wavelength and the refractive index of the medium.

$$L = \frac{4\ln(2)}{\pi n}\frac{\lambda^2}{\Delta\lambda} \qquad \text{(Eq. 2.6)}$$

Where L is the coherence length, n is the refractive index of the material, λ and Δλ are the center wavelength and the wavelength range of the light source, respectively. Interference occurs only when the path lengths of the two signals are matched within this length. Retrieving the data only from the interference signal allows data from a single depth to be selected. Hence, the coherence length corresponds to twice the axial resolution of the depth imaging.

This type of imaging system has been proven capable of generating very detailed 3-dimensional imaging of tissue. One common application for OCT is retinal imaging. The transparency of the human eye allows clear imaging of the retina, a critical diagnostic tool in opthamology (fig. 2.4). Figure 2.5 is another example of OCT image, in this case, utilizing focus tracking to maximize the spatial resolution throughout the image.

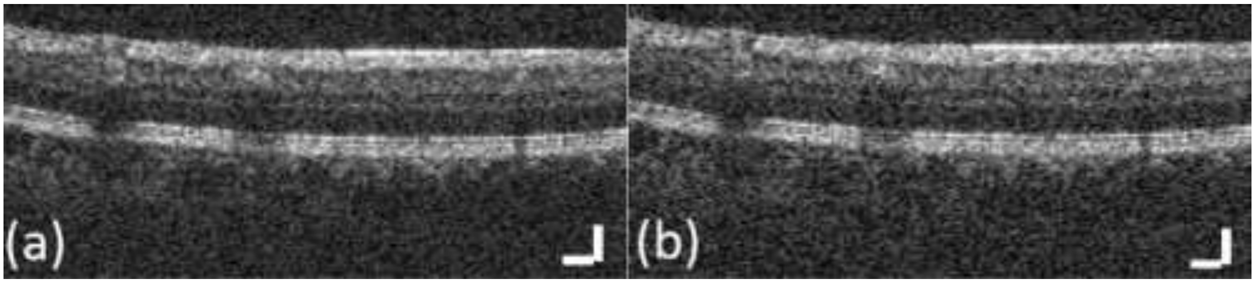

Fig. 2.4: Image of human retina obtained with an optical coherence tomography imaging system. [13]

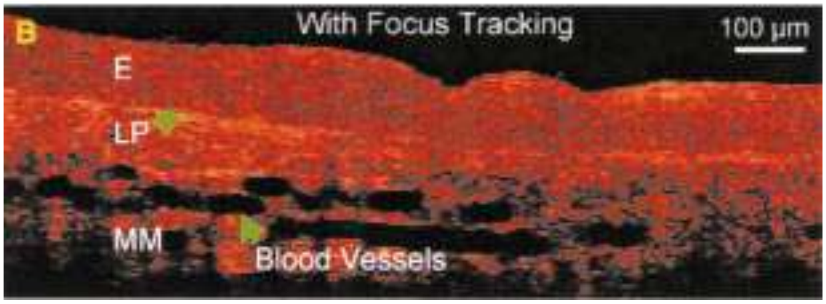

Fig. 2.5: Image of human tissue obtained with an optical coherence tomography imaging system, employing focus tracking to improve the lateral resolution throughout the image. [14]

2.3: MEMS Micromirrors for OCT

As mentioned in the previous section, one crucial component in the signal arm of the interferometer is a beam-steering device for image scanning. To acquire a full frame 3-dimensional image, 2-dimensional lateral scanning of the optical beam is necessary. This task is commonly achieved by using a set of two mirrors, each manipulated by a galvanometer. Each galvanometer mounted mirror allows scanning of the beam in one direction. Orthogonal positioning of these scanners enables 2-dimensional scanning of the beam. This setup is shown in fig. 2.6.

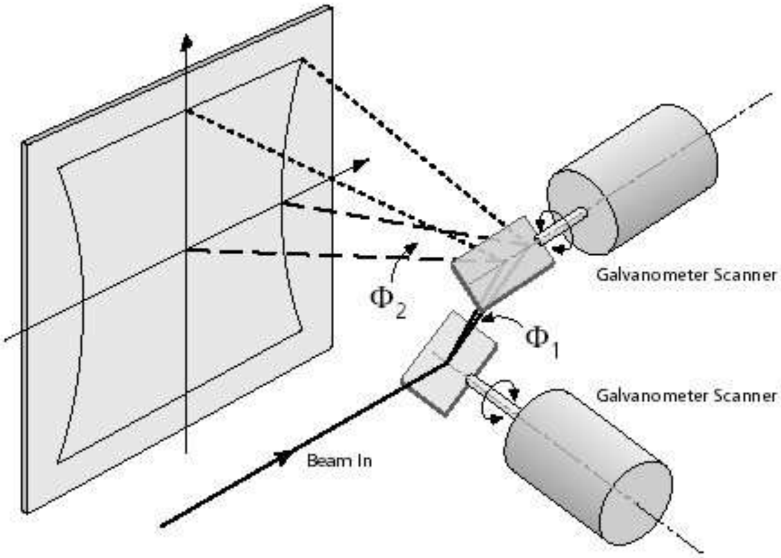

www.scanlab.de

Fig. 2.6: Conventional 2-dimentional OCT scanning system with 2 orthogonally positioned galvanometer mounted mirrors.

This setup is commonly used due to its simplicity and ease of use. This type of galvanometer has a linear scanning characteristic, can be actuated with low voltages, and has a linear response with respect to voltage. The main disadvantage of this setup is its physical dimensions. With each galvanometer being several centimeters in length, they cannot be integrated into endoscopic systems. Incorporation of MEMS micromirror devices into an OCT system, however, allows the size of the imaging probe to be drastically reduced. The functionality of two large galvanometers can be realized by a single flat scanning micromirror with a footprint smaller than 2 mm^2. This makes MEMS devices promising components for the implementation of OCT systems in endoscopic imaging applications.

MEMS micromirrors have been used for nearly every aspect of the imaging arm of the OCT system. Figure 2.7 shows an optical setup utilizing a MEMS device for focal control. A similarly positioned MEMS scanner device would enable spatial scanning of the optical beam.

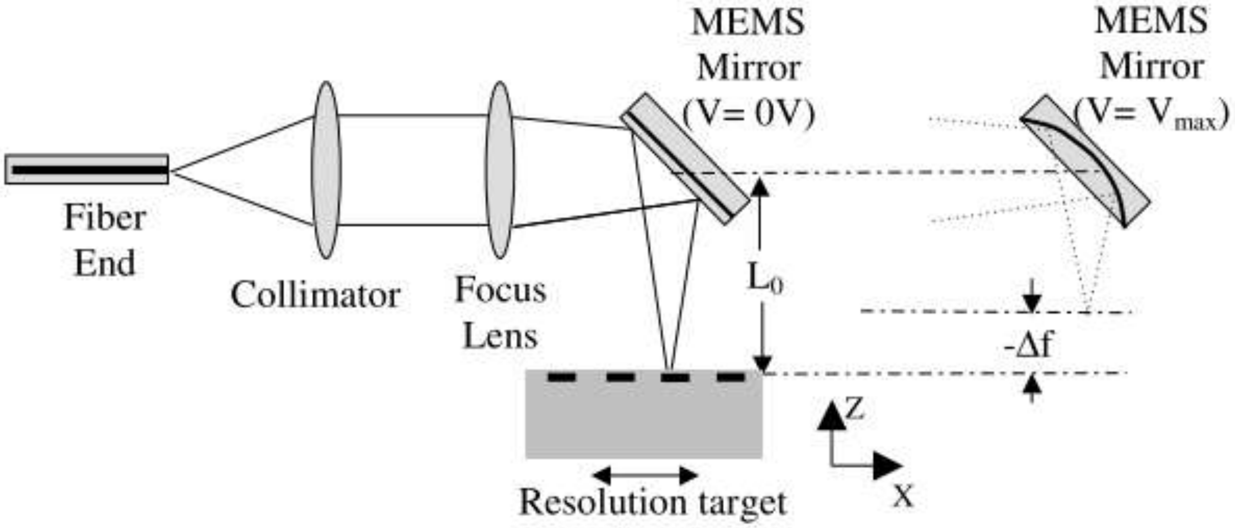

Fig. 2.7: Schematic of an imaging probe utilizing a deformable MEMS mirror to achieve focal tunability for OCT imaging. [24]

Scanning of the optical beam has been realized with several different designs of MEMS devices. Both 1-dimensional and 2-dimensional scanners have been developed, utilizing various actuation methods including piezoelectric, magnetic, thermal and electrostatic.

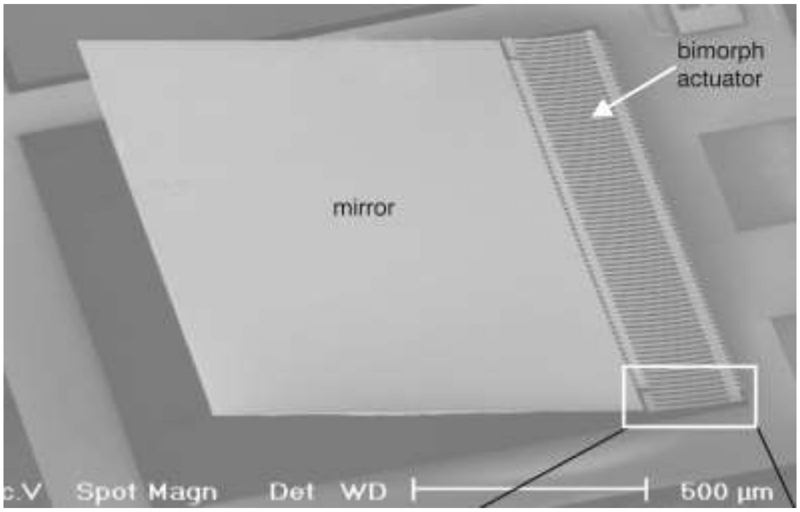

Fig. 2.8: 1-dimensional thermoelectrically actuated micromirror. [20]

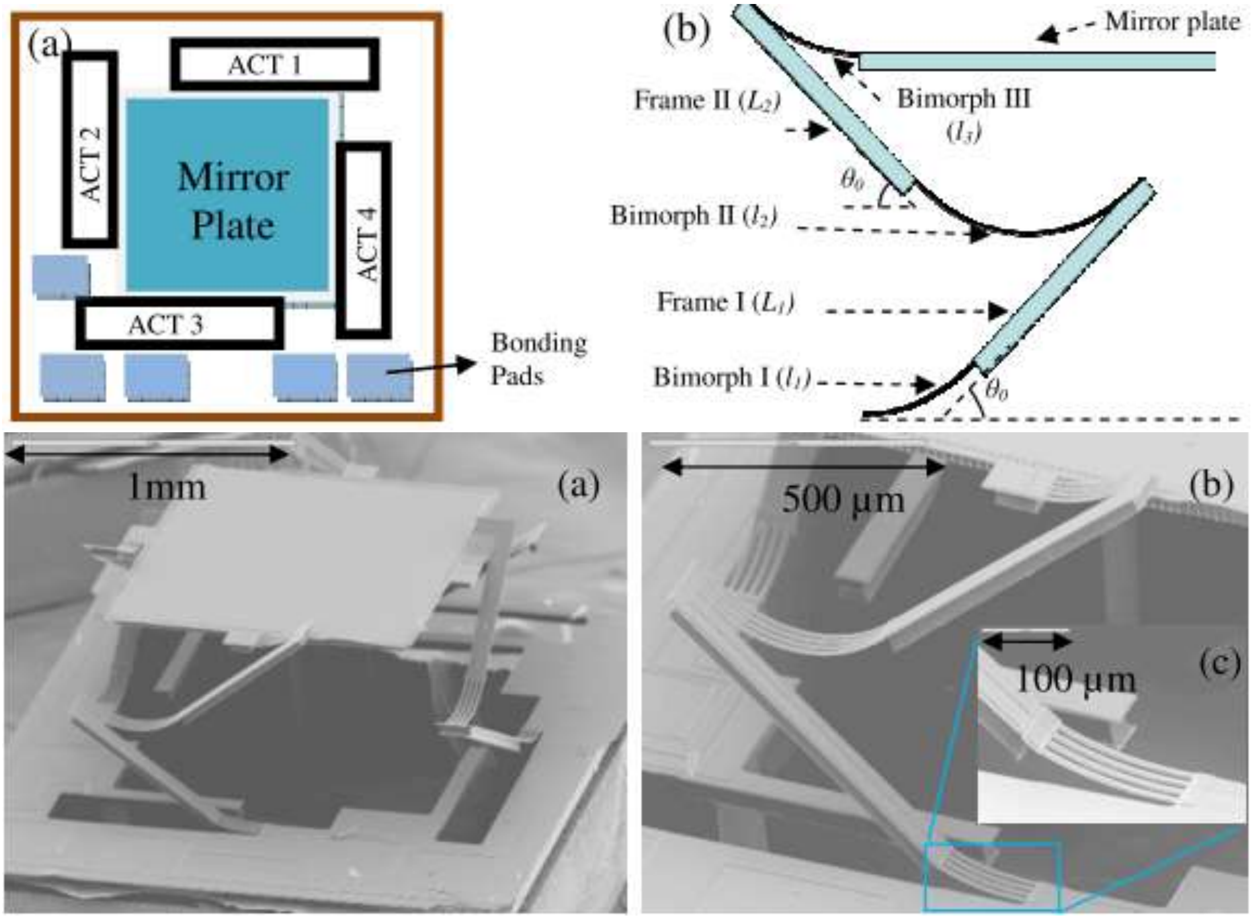

Fig. 2.9: Schematics (top) and scanning electron micrographs (bottom) of a 2-dimensional electrothermally actuated MEMS mirror. [8]

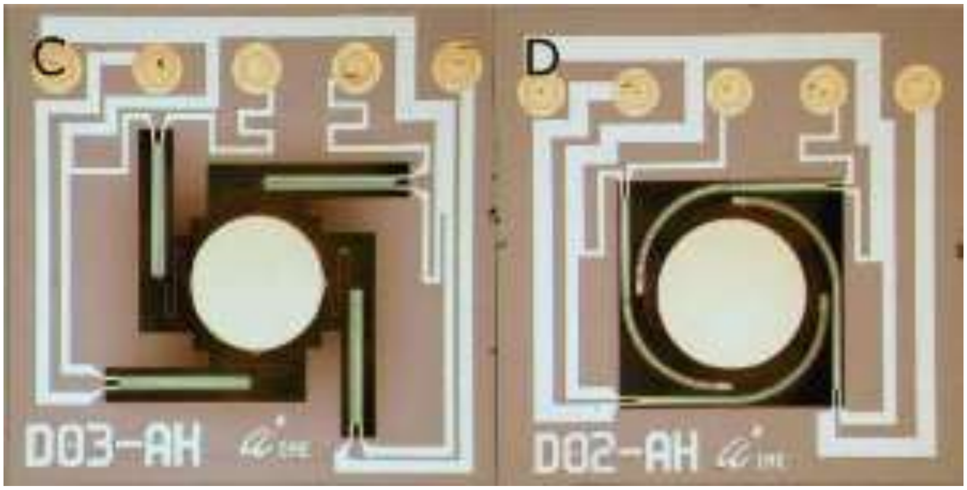

Fig. 2.10: Top-view optical microscope images of a 2-dimentional electrothermally actuated micromirror scanner. [25]

The devices shown in fig. 2.8, 2.9 and 2.10, are electrothermally actuated. This relies on a bimorph structure of materials with different coefficients of thermal expansion, causing the beam to bend when the temperature is changed. Because it is reliant on a change in temperature, electrothermal actuation generally requires higher actuation currents than other actuation methods and is slower in nature.

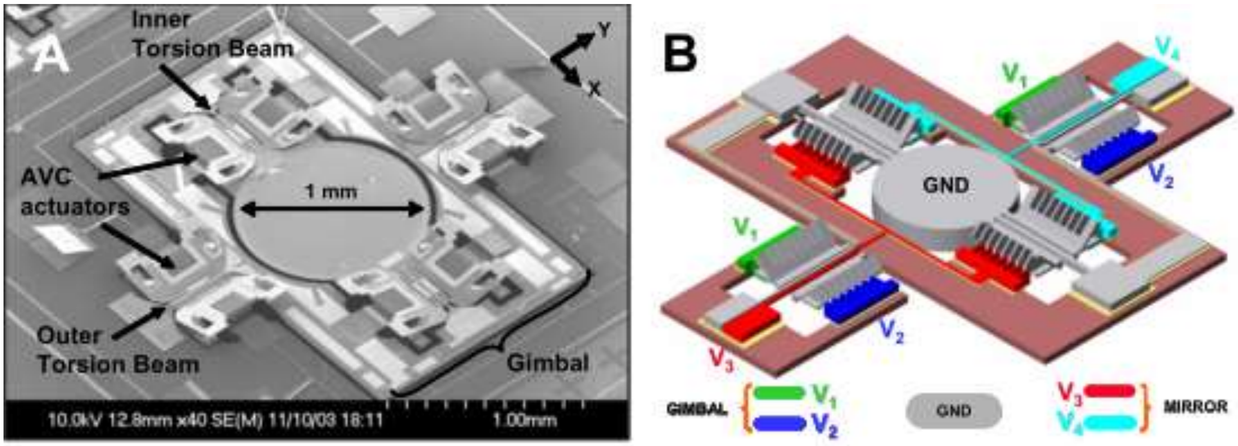

Fig. 2.11: 2-Dimensional electrostatically driven micromirror using torsional angled vertical comb actuators. [9]

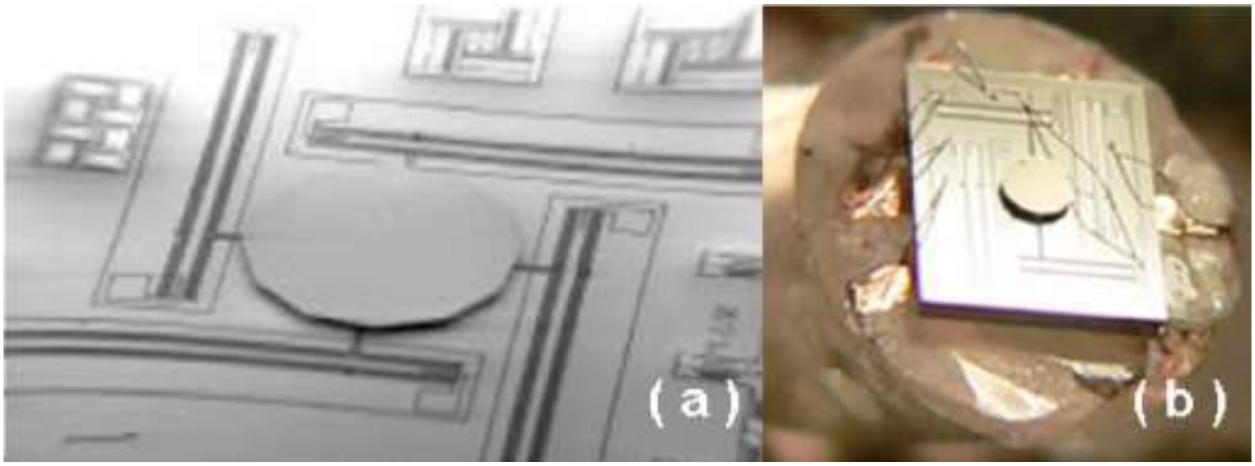

Fig. 2.12: 2-dimensional electrostatically actuated micromirror with a bonded mirror plate. [17]

Figures 2.11 and 2.12 show electrostatically actuated MEMS micromirror devices that use comb-drives. While the comb-drive geometry greatly decreases the necessary actuation voltages by increasing the electrode capacitance, they require a large amount of die space. The large size complicates their use in an endoscopic imaging system.

The main disadvantage of magnetically driven MEMS mirrors are the need of magnetic materials. The device shown in fig. 2.13, uses a small magnet that is attached to the underside of the mirror [18].

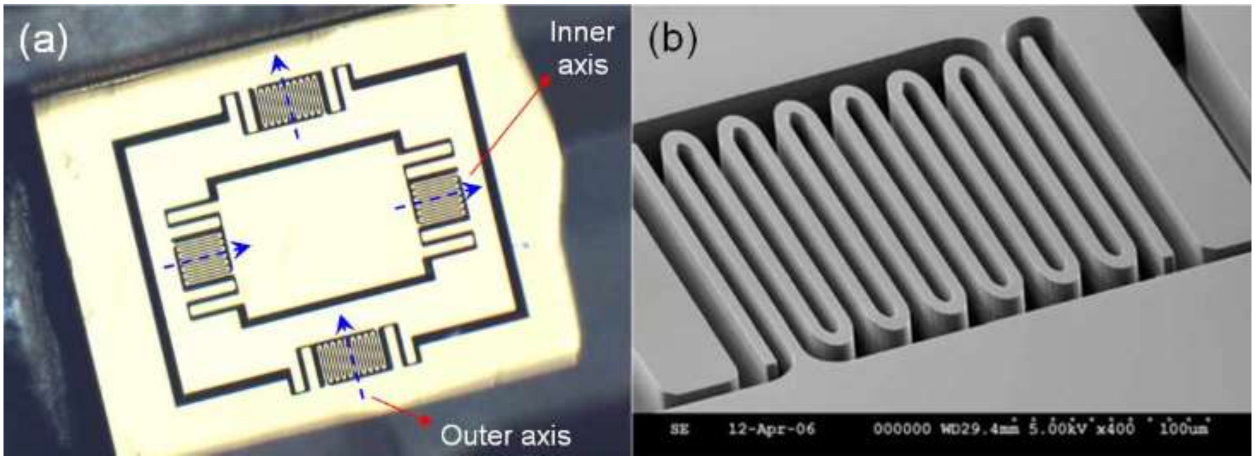

Fig. 2.13: Optical photograph (left) and scanning electron micrograph (right) of a 2-dimensional magnetically actuated MEMS micromirror. [18]

All of the devices shown here are examples of previous MEMS devices that were designed for use in OCT systems. An important consideration for endoscopic imaging applications is the fill factor, or the ratio of mirror area to die area. Electrostatically actuated MEMS devices using comb-drives are typically characterized by low fill factor due to the large size of the comb-drive actuators. Electrostatic actuation, however, is still attractive for this application due to the limited current in the system, caused only by leakage. Parallel plate electrode geometry can be used to preserve the low current characteristic and increase the fill factor.

In addition to beam scanning, MEMS devices have also been employed to achieve focus tracking in OCT systems. In traditional OCT systems, the focal length is fixed usually near the center of the target sample. This causes the lateral imaging resolution to degrade as the depth is increased. Focus tracking allows this resolution degradation to be avoided with dynamic control of the focal length of the reference arm. Similar to the different approaches for implementation of scanning capabilities in OCT systems, various designs have been realized for focus tracking. The two most common methods for dynamically controlling the focal length are tunable liquid lenses and deformable mirrors. A tunable lens can be achieved by controlling the pressure of a liquid trapped beneath a transparent stretchable membrane [26]. Figure 2.14 displays a cross-sectional schematic of a PDMS lens (left) and the packaged device (right). The same functionality can be achieved with a mirror membrane with a reflective surface suspended over a cavity (fig. 2.15) [24], [27]. In this type of device, actuation is achieved by applying an electric field between the mirror surface and an underlying electrode. This electric field creates a force between the two electrodes stretching and deforming the mirror membrane.

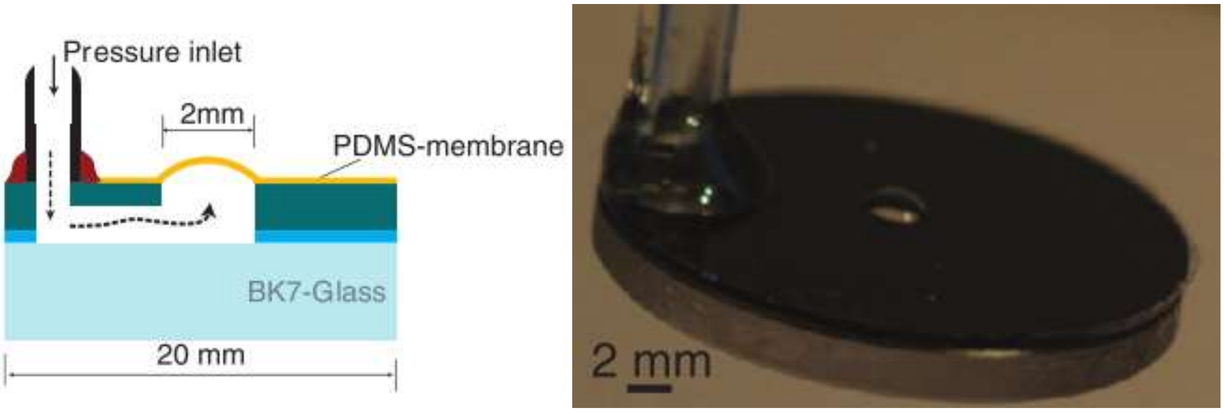

Fig. 2.14: A schematic of the pneumatically actuated micro-lens (left), an image of the completed lens device (right). [26]

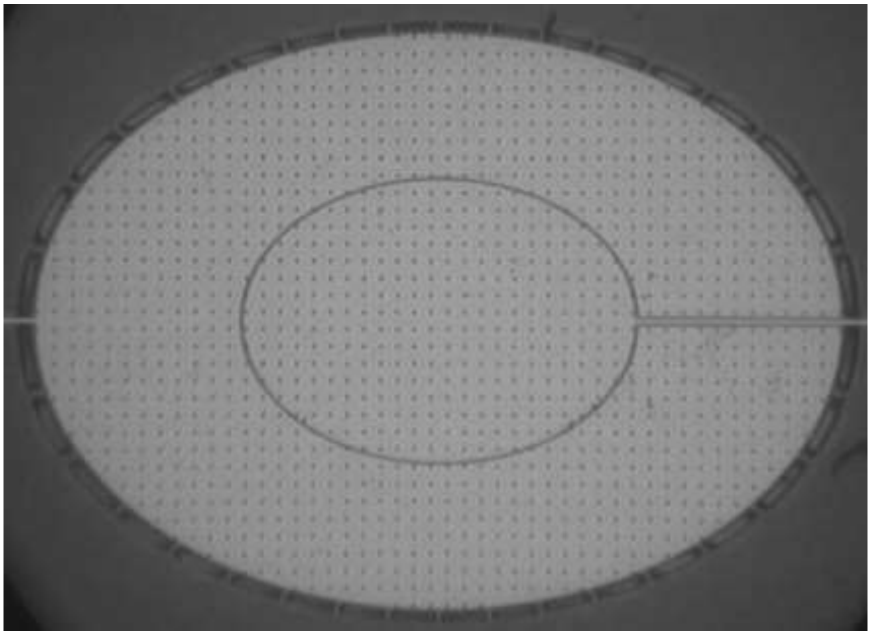

Fig. 2.15: Optical photograph of a deformable mirror capable of focus control. [24] The mirror is oblong because it was designed to be used at a 45 degree incident angle as shown in fig. 2.7.

The devices reviewed here have demonstrated the usefulness of MEMS devices for both 2-dimensional scanning and dynamic focus tracking. Integration of these two functionalities into a single MEMS device would be useful in many applications. Specifically for OCT, further miniaturization of the package size would be possible while retaining full scanning and focal control capabilities. For an endoscopic OCT imaging system, ideal characteristics for a MEMS scanning device would be as follows:

- Maximum fill factor for large reflective area
- Small device footprint to fit inside a 3 mm imaging probe
- Large scanning range for large field of view
- Linear spatial scanning for distortionless imaging
- Large focal range for maximum scanning depth
- Low actuation voltages
- High mechanical resonant frequency for fast angular repositioning

In the next chapter, the design of the MEMS scanning micromirror will be described with the trade-offs between these factors being considered.

Chapter 3: Device Design Considerations

As discussed in the previous chapter, control of the lateral position of the optical beam is necessary for the application of endoscopic OCT imaging. Additionally, dynamic control of the focal length of the imaging probe can improve overall image quality. MEMS technology enables the integration of both these functions into a very small package small enough to be included in an endoscopic imaging system. Of the various design considerations the first that needed to be determined was the method of device actuation.

There are several methods of actuation that are commonly employed in MEMS device including electrostatic, piezoelectric, magnetic, thermal actuation, etc. Determination of the best actuation method for a given application will be based on requirements for the specific device. The viability of each actuation method was considered for the application of endoscopic imaging. The main disadvantages of magnetic and piezoelectric actuation are their requirement of materials that possess specific material properties. While the realization of devices employing these actuation mechanisms that meet our specifications is possible, the benefits are outweighed by the increase in fabrication complexity.

Thermal actuation is very commonly used for MEMS actuation. One major advantage to thermal actuation is the large movement range of the actuator as compared to electrostatic actuation. Thermal actuation uses a 2-layer structure with the two materials having different coefficients of thermal expansion. When a current is passed through this type of structure, resistive heating results in mechanical stress between the layers, causing the structure to bend. However, resistive heating relies on high currents passing through the beams for actuation. The application of endoscopic imaging imposes stringent limits on the amount of electrical current that can be used in the body. This limitation reduces the attractiveness of thermally actuated devices for this application.

It was determined that electrostatic actuation was the most suitable choice for this device. Electrostatic actuation relies on the attractive force generated between two bodies when they are held at different electric potentials. This attraction can be explained using Coulomb's law which states that the electrostatic force experienced by two point charges is proportional to the product of the signed charges and inversely proportional to the square of the distance between them. This can be expressed as follows:

$$|\boldsymbol{F}| = k_e \frac{|q_1 q_2|}{d^2} \qquad \text{(Eq. 3.1)}$$

Where F is the magnitude of the electrostatic force, q_1 and q_2 are the magnitude of two point charges, d is the distance between the charges and k_e is Coulomb's constant. This relation can be utilized to describe the effect of a static voltage applied in a MEMS device. A linearly actuated MEMS type device with parallel plate electrodes is shown in fig. 3.1.

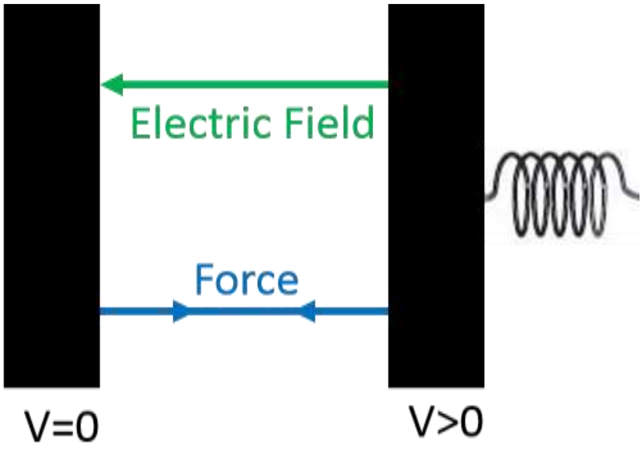

Fig. 3.1: Electrostatic attraction of a linear system with a spring supported electrode.

When a voltage is applied across the two electrodes, an electric field is produced. This electric field can be expressed simply as:

$$E = \frac{V}{d} \qquad \text{(Eq. 3.2)}$$

Where E is the electric field strength, V is the voltage applied to the electrodes and d is the distance between the electrodes. The force experienced by one of the electrodes can be calculated by differentiating the energy stored in the device capacitance with respect to the distance between the electrodes. Continuing with the assumption of a device with parallel electrodes this can be expressed as:

$$F_e = \frac{\partial}{\partial d}\left(\frac{1}{2}CV^2\right) = \frac{V^2}{2}\frac{\partial C}{\partial d} = \frac{\varepsilon A V^2}{2d^2} \qquad \text{(Eq. 3.3)}$$

In this expression F_e is the attractive force, C is the device capacitance, V is the applied voltage, d is the distance between the electrodes, ε is the permittivity of the gap material and A is the area of the electrodes. This, however, is derived for the simple case of parallel electrodes with linear movement perpendicular to the plane of the electrodes.

The desired MEMS device is a torsional mirror, with the tilt angle of the mirror being controllable. This necessitates the derivation of the torque generated on a device when actuated similarly as above. Figure 3.2 shows a simple diagram of a pivoting beam positioned above an electrode.

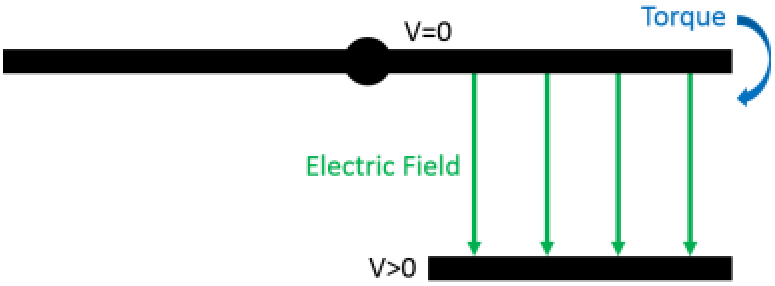

Fig. 3.2: Torsional operation of the micromirror when a voltage is applied.

For this type of device the electrostatic torque will be similar to the electrostatic force but the capacitance must be differentiated with respect to angular displacement:

$$T_e = \frac{\partial}{\partial \theta}\left(\frac{1}{2} C V^2\right) = \frac{V^2}{2}\frac{\partial C}{\partial \theta} \qquad \text{(Eq. 3.4)}$$

Where T_e is the electrostatic torque, θ is the angular displacement, C is the device capacitance and V is the applied voltage.

To analyze the mechanical aspects of the mirror, the geometry and material properties of the beams used to suspend the mirror must be considered. To allow for 2-dimensional scanning, the mirror is supported by two orthogonal sets of silicon nitride beams in our device design. This will be discussed in more detail later; for this discussion consider a mirror suspended by two beams on opposite sides of the mirror. When the mirror rotates along this axis, these beams will twist. This will induce a stress field in the material producing a torque in the opposite direction as the mirror deflection. This mechanical restoring torque provided by the beams will follow the rotational form of Hooke's law [28].

$$T_m = k \cdot \theta = \frac{2G_{SiN}T^3W}{3L}\left(1 - \frac{192}{\pi^5}\frac{T}{W}\tanh\left(\frac{\pi}{2}\frac{W}{T}\right)\right) \cdot \theta \qquad \text{(Eq. 3.5)}$$

This allows the calculation of the mechanical torque given the dimensions of the torsion bar (length, L, width, W and thickness, T), the shear modulus of silicon nitride, G_{SiN}, and the angular deflection of the MEMS mirror, θ. For this equation to hold it is assumed that the width of the beam is greater than its thickness.

During static actuation the device is at equilibrium, i.e. there is a zero net force and torque on the mirror plate. Because the linear movement of the device is negligible compared to the rotational movement, the forces can be neglected. Hence, only the electrostatic torque produced by the actuation voltage and the restoring torque produced by the torsion springs supporting the mirror have to be considered. At equilibrium, the mechanical torque must be equal in magnitude to the electrostatic torque while being opposite in direction. Using this equality, it is possible to calculate the angular deflection of the mirror given an applied DC voltage. However, it is difficult to calculate the electrostatic torque directly because the capacitance in the expression changes nonlinearly with respect to the angular deflection. To complete these calculations and gain valuable insight into the behavior of the device a mathematical simulation program was written to calculate the tilt of the micromirror under static actuation. The simulator was designed to determine the significance of various geometric properties of the mirror with quick simulation of the system while varying a parameter of interest.

This simulation program allowed optimization of several elements of the design. The optimal spacing between the mirror and electrodes was determined, electrode geometries optimized, and scanning effects of various device parameters characterized. Early failure, from snap down, limited the scanning range of prototype devices. To reduce the force causing this premature failure, the electrode geometry was altered to remove area from the center of the mirror where very little torque was produced. Without tilt the force between the mirror and the electrodes is uniform across the electrode area, but the torque produced at the edge of the mirror is much greater than at the center. To improve the device behavior, the center most parts of the electrodes were etched away (fig. 3.3). This allowed nearly as much torque to be generated while reducing the linear force pulling the mirror vertically. Figure 3.4(a) shows deflection versus voltage curves for the altered electrode geometries. An electrode etchback distance of 200 µm was chosen because of the negligible increase in actuation voltage.

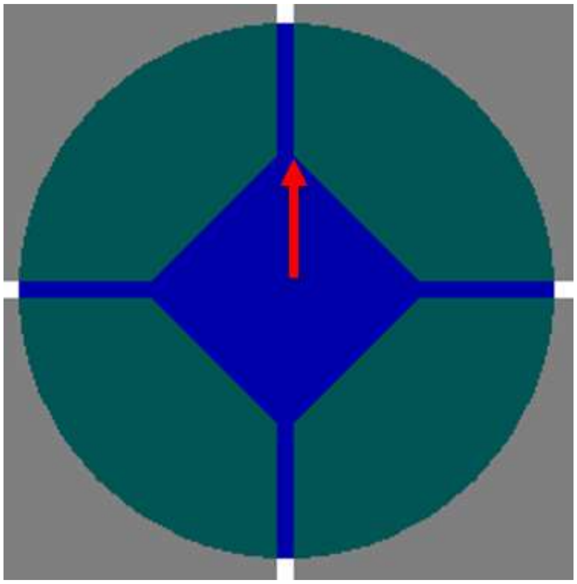

Fig. 3.3: To reduce the linear downward force on the mirrors the center corners of the underlying electrodes were etched away. The blue circle shows the outline of the mirror and the grey areas are the underlying electrodes. The red arrow indicates the direction in which the etch distance was measured.

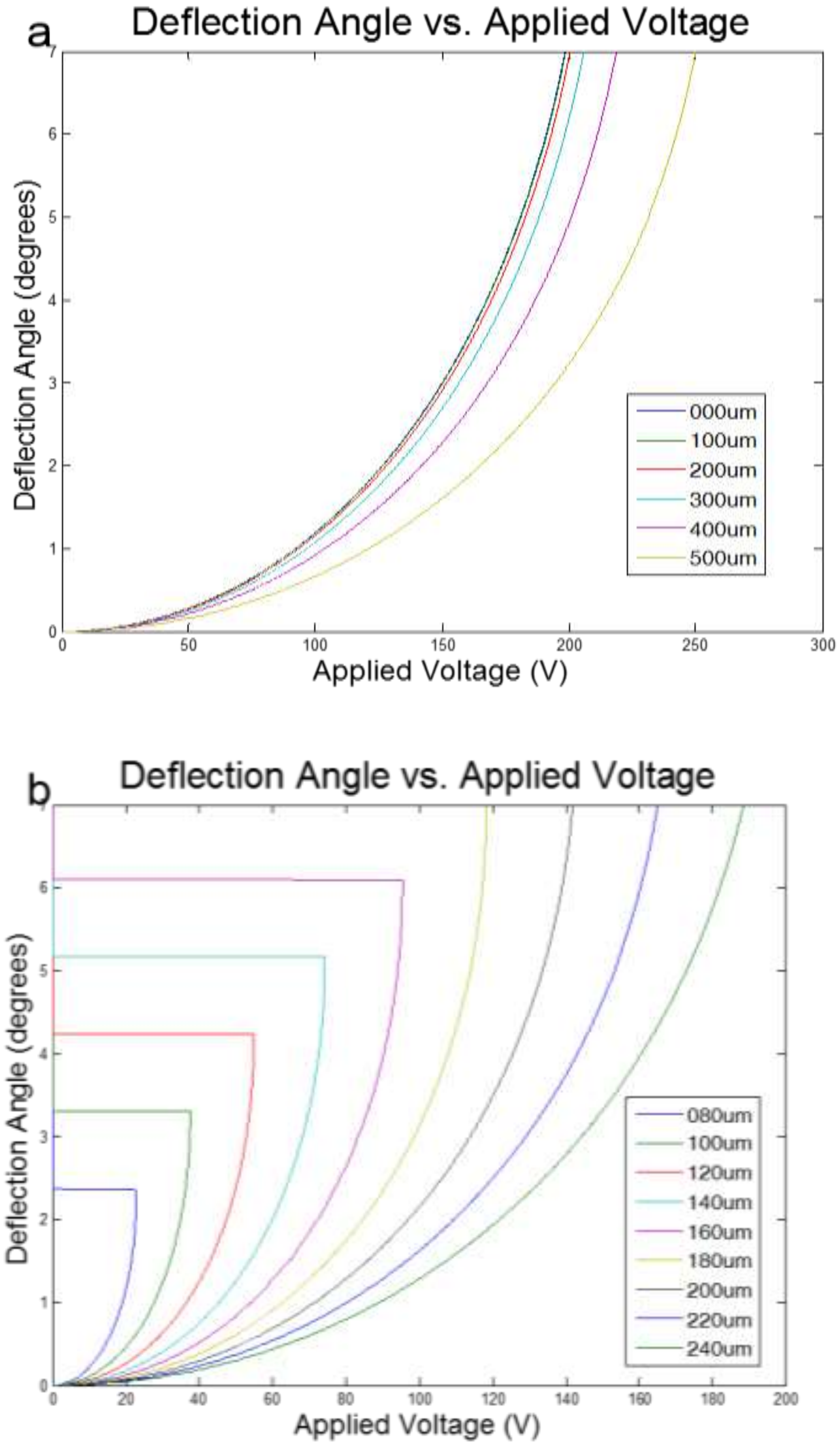

Fig. 3.4: Simulated deflection angle versus voltage curves with varying electrode etch distances (a) and device to electrode separation (b).

Another common problem associated with MEMS devices is snap down. This phenomenon occurs when the force on the device is too great and a moving part gets pulled down into contact with the actuation electrode, commonly destroying the device. For these micromirror devices snap down occurs when the electrostatic torque increases faster than the mechanical torque for a given deflection angle or:

$$\left|\frac{\partial T_m}{\partial \theta}\right| < \left|\frac{\partial T_e}{\partial \theta}\right| \qquad \text{(Eq. 3.6)}$$

Alternatively, this is also the point at which the voltage necessary to hold the mirror at an increasing angle begins to decrease, or:

$$\frac{\partial V}{\partial \theta} < 0 \qquad \text{(Eq. 3.7)}$$

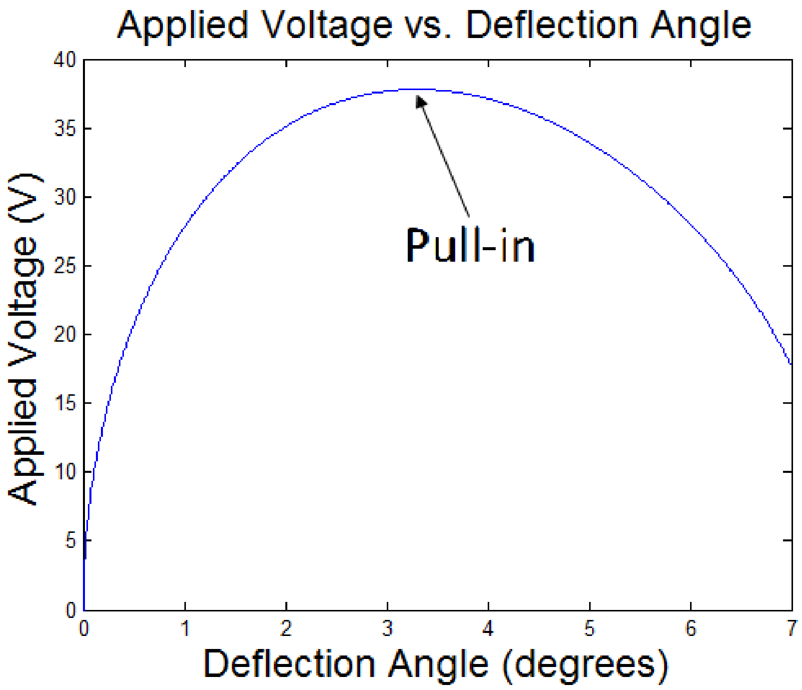

Fig. 3.5: Device pull-in occurs when the voltage required to hold the mirror at an increasing deflection angle decreases. This point is shown in a curve of applied voltage versus deflection angle.

Because the mechanical torque is almost linear, snap down will always eventually occur as the voltage and angular deflection increase. This point is difficult to calculate directly but easily identifiable from the simulation results. Figure 3.4(b) displays the reflection angle of the device as a function of the applied voltage and the electrode spacing. The snap down condition is represented by the horizontal lines back to the Y-axis. The point of snap down represents the absolute maximum scanning angle achievable with static actuation and a given electrode geometry. Using these types of curves it was possible to determine the optimal air gap between the mirror and electrodes to minimize the actuation voltages while still allowing for the desired maximum deflection. The optimal separation distance was determined to be around 180 µm.

In addition to the characterization of the static actuation of the MEMS micromirrors, derivation of the behavior of the mirrors at resonance was investigated. When actuating with a voltage signal with a frequency tuned to the mechanical resonance of the MEMS device, the mirror is never at rest and therefore the balance between the electrostatic and mechanical torques discussed previously for DC actuated mirrors does not exist. Rather, the system is characterized by an equilibrium between potential and kinetic energy, and also between energy introduced to the system through actuation, and energy dissipated during one period of mirror movement. In an ideal system without mechanical losses, during each half period of the mirror's scan the mechanical potential energy is converted into kinetic energy and back into potential energy but with the opposite magnitude. In an undamped system this oscillation would persist indefinitely; however, in a real system, energy is dissipated each cycle due to mechanical losses. At equilibrium, in a real system, the energy lost per cycle must be balanced by the energy that is introduced into the system through electrostatic actuation. The energy added to the system can be expressed as:

$$Energy\ added \propto \frac{V^2}{2}(C_2 - C_1) \qquad \text{(Eq. 3.8)}$$

Where V is the voltage applied to the electrodes and C_1 and C_2 are the capacitances at the beginning and end of the half cycle. The quality factor for the device is a constant that related to the resonance peak. It can be expressed as:

$$Q = 2\pi \frac{Energy\ Stored}{Energy\ Dissipated\ per\ cycle} \qquad \text{(Eq. 3.9)}$$

The energy stored in the device is equal to the mechanical potential energy stored in the torsion springs when the mirror is at maximum angular deflection. Similar to a linear spring, the energy stored in a rotational spring system is:

$$U = \frac{k \cdot \theta^2}{2} \tag{Eq. 3.10}$$

Knowing that the energy added to the system is equal to the energy dissipated during each cycle, it can be shown, from equations 3.8 and 3.9, that:

$$V^2(C_2 - C_1) \propto k \cdot \theta^2 \tag{Eq. 3.11}$$

From equation 3.11, it is clear that the voltage squared is proportional to the angular deflection squared. This shows a clear linear relationship between the deflection of the micromirror at resonance and the voltage applied.

With the operating principles of the device set, further design of the specific device parameters was possible. A mirror diameter of 800 μm is sufficiently large to reflect all of the incident light while remaining small enough to fit in the endoscope. While the size limitation is, perhaps, the most important consideration, the size of the mirror also affects other operational parameters. As the mirror size increases, the necessary actuation voltages will drop due to the increase in device capacitance. Additionally, the resonant frequency of the mirror will decrease due to its dependence on the moment of inertia, and therefore, mass. The circular shape of the mirror ensures its curvature to be spherical when the membrane is stretched to modify the focal length. A gimbaled structure with two orthogonal pairs of torsion beams is used to allow tilting of the mirror in any direction. As discussed above the device is electrostatically actuated. This actuation method requires six electrodes for complete control of the mirror. Two electrodes are on the mirror device itself and four are patterned on a secondary wafer, positioned beneath the device wafer. The electrodes on the mirror are responsible for the focal control, the first being the reflective metal layer on the membrane and the second being the conductive silicon frame that supports the membrane. Vias etched through the silicon nitride layer allow charge to be routed to the underlying silicon which is grounded for testing. Each of the four electrodes beneath the mirror can be charged to tilt the mirror toward that electrode. A cross-sectional view of this device showing its structure and 2 of the 4 underlying electrodes is displayed in fig. 3.6.

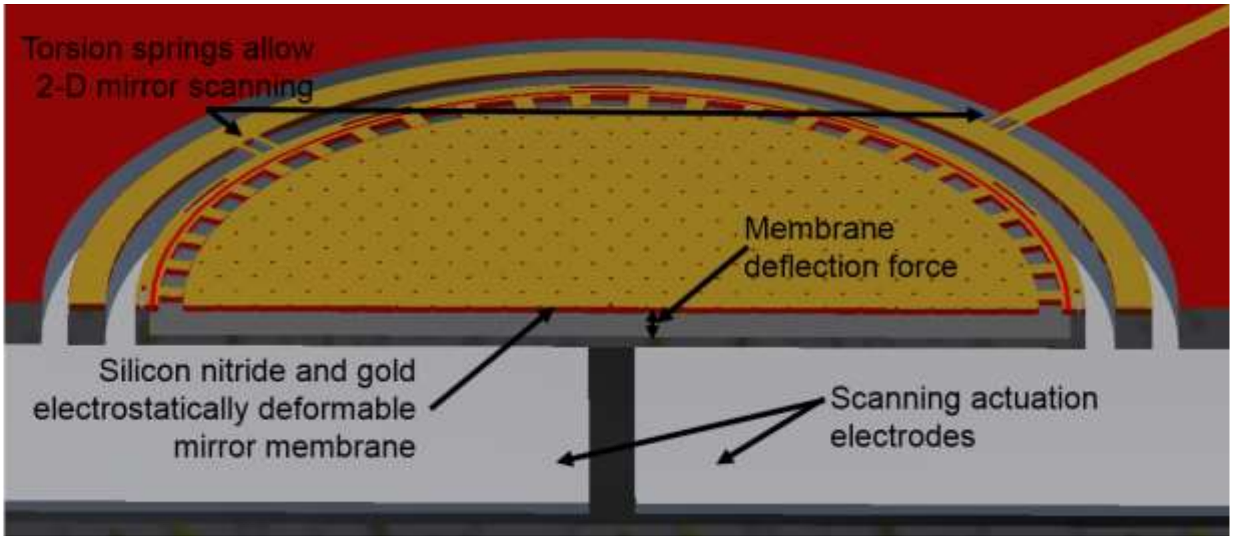

Fig. 3.6: Cross-section of the 3-dimensional MEMS scanner. The mirror device is suspended above a set of 4 aluminum electrodes (only 2 shown) that allow tilting of the mirror. The curvature is controlled by applying a potential between the gold mirror surface and the silicon mirror frame. [29]

Chapter 4: 3-Dimensional MEMS micromirror scanner

4.1: Device Fabrication

In the pursuit of realizing a MEMS micromirror device that integrated spatial scanning with focal control, simplified devices demonstrating the scanning capability and curvature control, separately, were initially developed with vastly similar fabrication procedures. The development of these initial device structures expedited the overall development of the final mirrors by allowing the development and optimization of much of the fabrication process with simpler test structures. These test structures could be produced more quickly and at lower cost.

4.1.1: Curvature Controllable MEMS Micromirrors

The first devices that were developed were simplified mirror devices with electrostatic curvature control. The device structure includes an etched silicon cavity beneath a silicon nitride membrane with a chrome (Cr)/gold (Au) reflective layer (fig. 4.1).

Fig. 4.1: Cross-sectional drawing of the curvature controllable devices with a released Au and silicon nitride membrane.

The fabrication process (fig. 4.2) begins with a highly doped silicon wafer. The doping is necessary to reduce the resistivity of the silicon to facilitate conduction in the underlying silicon frame that acts as one of the actuation electrodes. A ~580 nm silicon oxide layer is grown on the substrate using wet thermal oxidation. This layer is patterned using contact photolithography to create the silicon oxide pads beneath the mirror membrane. The pattern is transferred into the silicon oxide layer through reactive ion etching (RIE) in a CHF_3/CF_4 chemistry (fig. 4.2(a)). The wafer is then cleaned with a standard RCA cleaning procedure and a 500 nm silicon nitride layer is deposited using low pressure chemical vapor deposition (LPCVD) (fig. 4.2(b)). Electrical vias are patterned and etched through the silicon nitride to the underlying silicon, using RIE, to facilitate electrical conduction to the silicon electrode. A magnetron sputter system is used to deposit the Cr adhesion layer and the reflective Au electrode layer (fig. 4.2(c)). After photolithography, the Au and Cr layers are etched in corresponding commercial wet etchants from Transene. The patterning of this metal layer allows independent routing of charge to the underlying silicon and the membrane electrodes. The final step in the process is the release of the membrane. Reactive ion etching (RIE) using SF_6 is then used to etch through the silicon nitride layer (fig. 4.2(d)). The sacrificial silicon oxide layer is etched in 49% hydrofluoric acid (HF) (fig. 4.2(e)). This sacrificial layer is necessary to allow the even and complete etching of the silicon beneath the membrane. Finally, the membrane is released by etching the underlying silicon in a 30% potassium hydroxide (KOH) solution at 80°C. A cross sectional view of the completed device is shown in fig. 4.2(f).

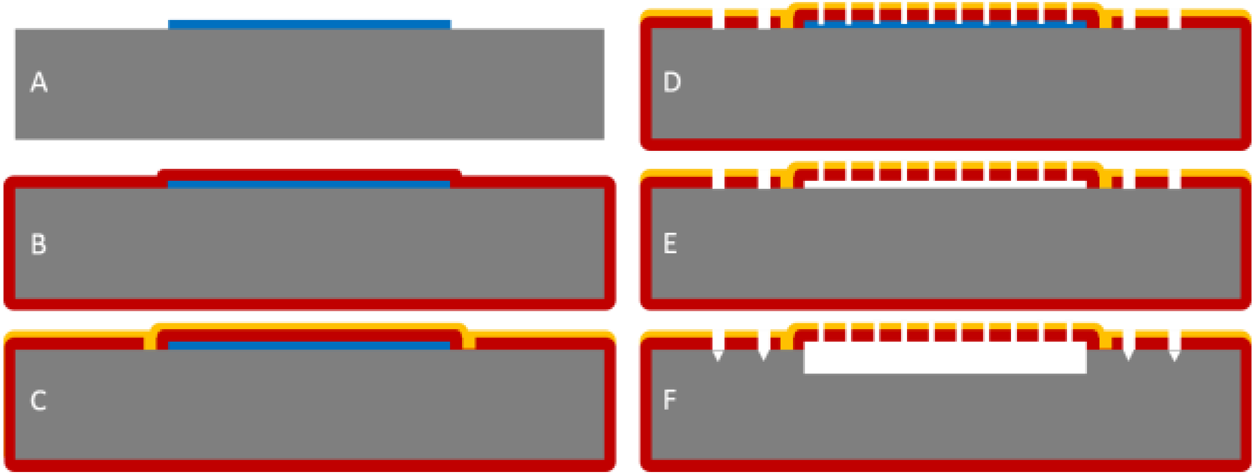

Fig 4.2: (A) A double side polished is oxidized and silicon oxide pads are patterned (B) LPCVD is used to deposit a conformal silicon nitride (C) Electrical vias are etched through the nitride and the wafer is metallized (D) The gold, chrome and silicon nitride are etched (E) Hydrofluoric acid is used to etch the sacrificial silicon oxide layer. (F) KOH is used to etch a cavity in the silicon and finish the release of the device.

4.1.2: 2-Dimensional MEMS Scanner

The fabrication process for the scanning only devices was developed alongside the curvature control devices. To keep the fabrication procedures consistent, the thin film stack and process are very similar between the two process flows with some small differences. For these devices, with processing carried out on both sides of the substrate, a double side polished silicon wafer is used (fig. 4.3(a)). As in the previous process, the silicon is highly doped for good conductivity. The silicon oxide layer used in the previous process facilitates the release of the membrane and therefore it is not necessary in this process. Hence, the first step is the LPCVD deposition of the silicon nitride layer (fig. 4.3(b)). Unlike the previous process, the silicon in the vicinity of the mirror must be thinned to allow for the final release. This is accomplished by patterning the silicon nitride on the backside of the wafer before KOH etching of the silicon to a thickness of ~30-40 micrometers (fig. 4.3(c)). The electrical vias are etched through the silicon nitride layer on the front side of the wafer, and the Cr/Au reflective layer is sputter deposited as described previously (fig. 4.3(d)). The release of this device is accomplished in several steps. Firstly, the Au and Cr layers are chemically etched. RIE is then used to etch through the silicon nitride layer to the silicon. Deep reactive ion etching (DRIE) is used to etch trenches in the silicon defining the gimbaled structure and the mirror tethers (fig. 4.3(e)). The final release of the device is completed in another KOH etch. This finalizes the through-wafer etch as well as undercutting the silicon nitride tethers (fig. 4.3(f)).

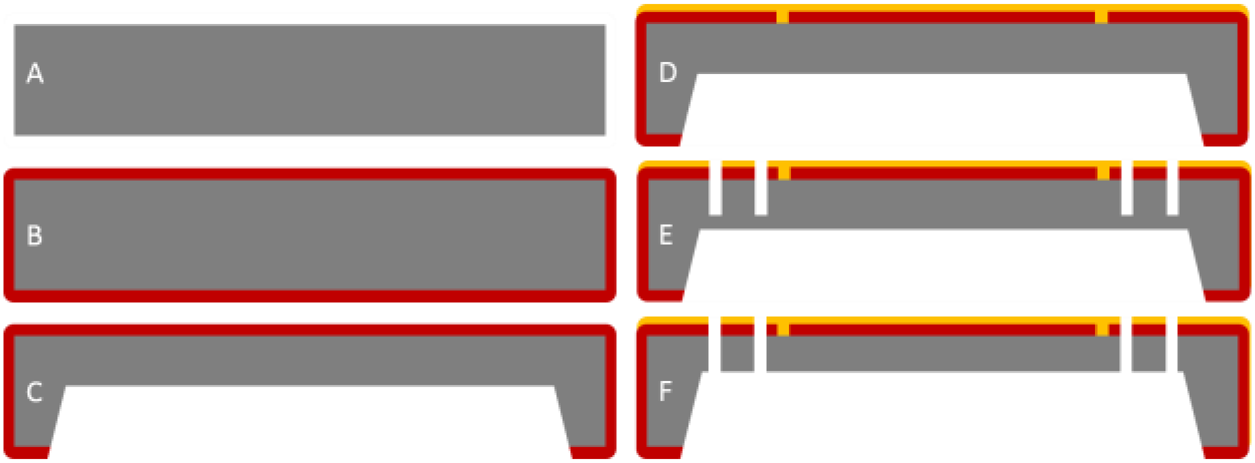

Fig 4.3: (A) A double side polished silicon wafer (B) LPCVD is used to deposit a conformal silicon nitride (C) The backside of the wafer is patterned and KOH is used to thin the silicon wafer in the area of each mirror (D) Electrical vias are etched through the silicon nitride before the wafer is metallized (E) The metals and silicon nitride are etched before trenches are etched into the silicon (F) KOH is used to finish the release of the device.

4.1.3: 2-Dimensional MEMS Scanner with Focal Control

The 3-dimensional scanning devices integrate the functionality of the previous two designs into a single device. The design included integrating the cavity, allowing curvature control, into the scanning devices. While the two separate process follow largely the same process flow and utilized nearly identical thin film stacks, merging the two fabrication schemes into a single process flow presented new difficulties.

Fig 4.4: Cross-sectional drawing of the finished 3-dimensional scanning MEMS mirror with released Au/silicon nitride membrane and Au/silicon nitride/silicon gimbal.

The main modification necessary in the flow is the final KOH etch time for the release of the devices. For the scanning devices, the optimal etch time for this release was very short, less than 5 minutes, to minimize the damage done to the gimbal due to undercutting of the silicon nitride layer. However, the devices with curvature control did not present this issue, and therefore the optimal release time was much longer to allow for the cavity beneath the mirror to be sufficiently etched (up to 30 min). The location of interest for these two aspects of the release etch are visible in fig 4.5.

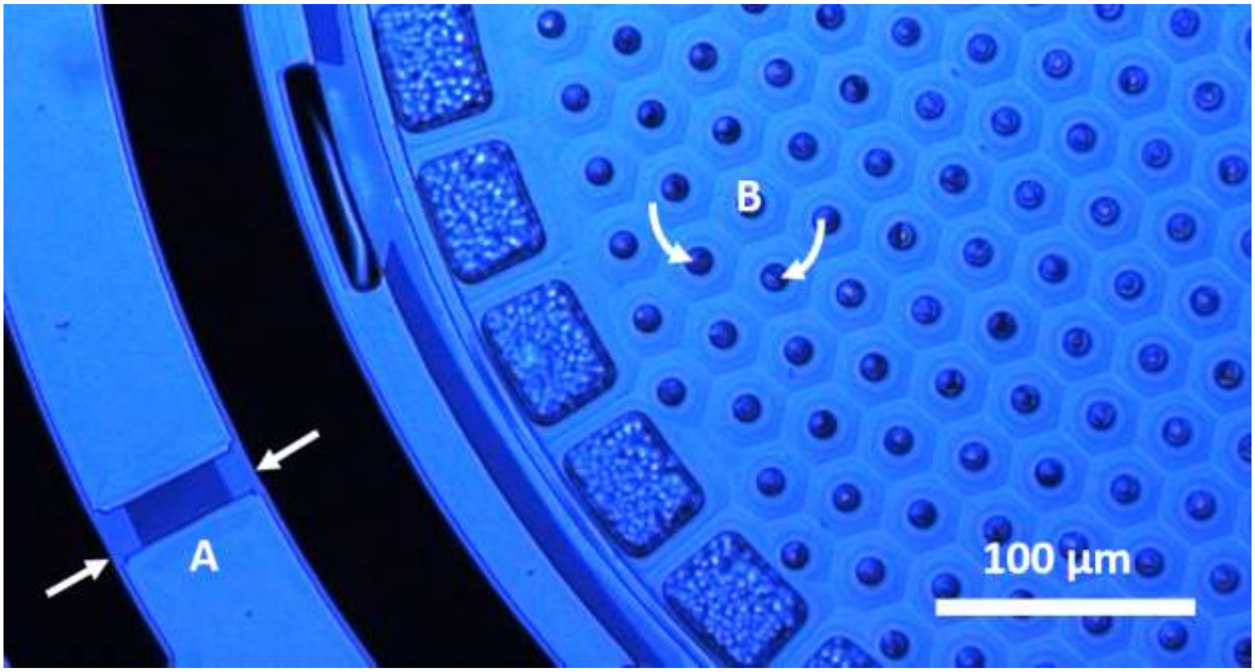

Fig 4.5: During release, undercutting of the gimbal occurs (a). Progression of the membrane release relies on chemical transport through etch vias on the surface of the mirror (b).

One possible solution to this problem is to increase the speed of the etch to create the cavity. This can only be accomplished, however, by an increase in the chemical transport to the surface to be etched. For our devices this could only be accomplished by increasing the amount or size of the etch vias on the surface of the mirror. Because the membrane also acts as the reflective surface for the mirror, this would also worsen the mirror's performance by increasing the diffractive losses. With the density of the vias slightly increased and the mirror's gimbal redesigned and enlarged, an etch time was possible that allowed the full release of the membrane without undercutting and destroying the gimbal.

The fabrication process for the fully functional MEMS micromirrors is a five photomask process that starts with a silicon wafer that is polished on both sides and highly doped for good electrical conductivity. A ~580 nm silicon oxide layer is grown with wet thermal oxidation at

1050°C. This layer is patterned to form the sacrificial pads beneath each mirror (Fig. 4.6(b)). Low pressure chemical vapor deposition (LPCVD) is then used to deposit the 500 nm silicon nitride membrane layer (Fig. 4.6(c)). The nitride on the backside of the wafer is then patterned with the second photomask and deep (~470µm) windows are etched into the wafer using KOH (Fig. 4.6(d)). These windows thin the bulk silicon layer to about 30-40µm thick at the location of each mirror. The next photomask defines the electrical vias and this pattern is etched through the silicon nitride to the silicon. A 200nm Au layer and a thin Cr adhesion layer are then sputter deposited after a short argon plasma treatment (Fig. 4.6(e)). The argon plasma treatment serves two purposes: it removes any native oxide that may remain on the silicon and roughens the wafer’s surface to promote the adhesion of the metal layer. The fourth photomask defines the electrical traces on the wafer and creates selected metal cuts on the mirror and gimbal. Commercially available wet metal etchants from Transene are used to etch the Cr (nitric acid and ceric ammonium nitrate) and Au (iodine complex and potassium iodide) metal layers. The final photomask defines the trenches creating the gimbal and the etch vias in the surface of the mirror. After this lithography step, the metal layers are etched again and the pattern is etched through the nitride layer. DRIE is then used to transfer the pattern into the silicon defining the gimbal and the resist is removed (Fig. 4.6(f)). The silicon oxide pad beneath the mirror surface masks the underlying silicon to prevent etching of the mirror structure. During the final wet etching release of the devices they become extremely delicate and must be handled gently. First, HF is used to etch the sacrificial oxide under the membrane (Fig. 4.6(g)). Then a KOH etch enlarges the cavity beneath the membrane and completely releases the device by finalizing the through wafer etch and undercutting the torsion springs. To reduce the risk of the membranes snapping in while drying they are submerged in isopropyl alcohol before being allowed to dry. A cross sectional view of the final released devices is shown in fig. 4.6(h). An optical image and a scanning electron micrograph of the finished devices can be seen in fig. 4.7.

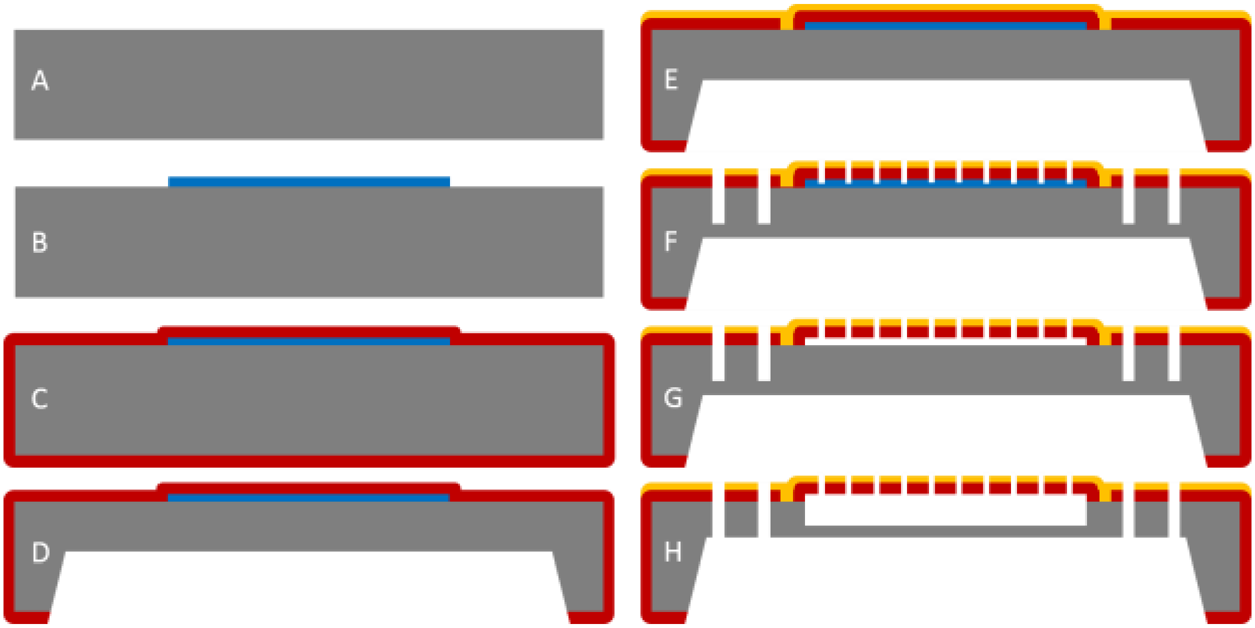

Fig 4.6: (A) A double side polished silicon wafer (B) The wafer is oxidized and silicon oxide pads are patterned (C) LPCVD is used to deposit a conformal silicon nitride (D) The backside is patterned and the silicon is thinned in the area of the mirrors (E) Electrical vias are etched through the nitride and the wafer is metallized (F) The gold, chrome and silicon nitride are etched before trenches are etched into the silicon (G) Hydrofluoric acid is used to etch the sacrificial silicon oxide layer. (H) KOH is used to etch a cavity in the silicon and finish the release of the device.

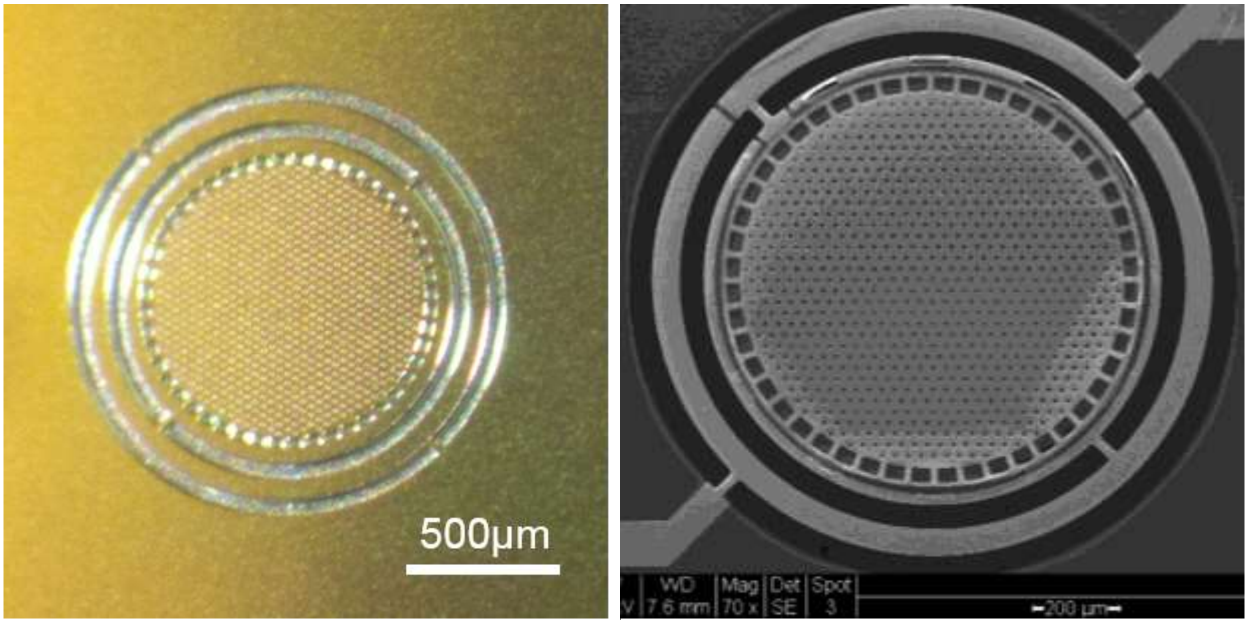

Fig 4.7: An optical microscope photograph (left) and a scanning electron micrograph (right) of a fabricated MEMS micromirror device.

4.1.4: Actuation Electrodes

In addition to the fabrication of the actual MEMS devices, a set of electrodes is fabricated on a separate wafer. After fabrication, these electrodes will be positioned beneath the devices to allow electrostatic control of the mirror's tilt in any direction. Because the amount of electrostatic actuation achieved is related to the magnitude of the electric field, and therefore depends on the separation between the two charged electrodes, the electrodes must be fabricated on raised pillars that fit into the cavities etched in the backside of the device wafer. Etching of these pillars is achieved using KOH etching of single crystal silicon, now taking advantage of the anisotropic nature of the etch. The KOH etch progresses at a different rate for each exposed crystal plane, with the (100) and (110) crystal planes etching significantly faster than the (111) plane [30]. This causes convex corners to be etched at a much higher rate than flat surfaces or concave corners, which causes undercutting. This behavior is not significant in the fabrication of the mirror structures due to the mask geometry including only concave corners. Etching of the pillar structures, however, necessitates convex corners. To account for the accelerated etching of these corners, a technique called corner compensation can be used [31]. To achieve convex corners, extra masking material must be assigned to the convex corners. As the etch progresses this extra material is etched away leaving the desired structure intact. In our case large square regions were added to the corners of the pillars to protect the convex corners. The progression of this etch is shown in fig. 4.8.

Fig 4.8: Corner compensation allows protection of the convex corners of the silicon pillars during the progression of the KOH silicon etch. The layout design of the silicon nitride mask (left), an image a partially etched pillar with the undercut silicon nitride mask still visible (center) and the fully etched silicon pillar with an insulating oxide layer (right).

The fabrication for the electrodes begins with an extra thick (1 mm thickness) silicon wafer. After cleaning the wafer, plasma-enhanced chemical vapor deposition (PECVD) is used to deposit silicon nitride on both the top and bottom surfaces of the wafer. This silicon nitride layer is then patterned and etched using RIE. After removal of the photoresist, KOH is used to etch the silicon creating 400 µm high silicon pillars. A thick, ~2 µm, silicon oxide layer is deposited on the wafer to electrically isolate the silicon. 400 nm of aluminum is then sputter deposited, the conformal deposition providing conduction to the top plane of the pillars. Because of the large, out-of-plane structures on the wafer at this point in the fabrication process, conventional spin coating of photoresist cannot be used. Instead, the photoresist is spray coated in several layers, providing a very conformal layer on the entire wafer surface including the pillar sidewalls. The wafer is then exposed and the pattern developed. The final step in this process is the wet etch of the aluminum and the removal of the photoresist. Figure 4.9 shows the raised electrodes that have been fabricated.

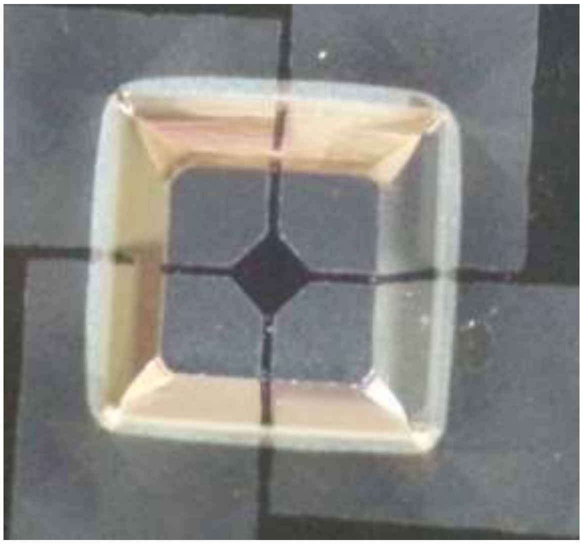

Fig 4.9: A finished silicon pillar with patterned aluminum electrodes. The ~400 µm tall pillar decreases the necessary actuation voltages by increasing the capacitance due to the mirror's proximity to the electrodes.

Following the fabrication of the pillar electrodes assembly of the final devices is completed by aligning the two wafers, via optical alignment, and bonding them. A cross-sectional drawing of a finished micromirror device mounted on the raised electrodes is shown in figure 4.10.

Fig 4.10: A Cross-section view of the 3-dimensional micromirror device with underlying aluminum electrodes.

4.2: MEMS Device Testing

The micromirror devices were tested in multiple ways to characterize their performance. The two major components of the testing included measurement of the focal controllability and the scanning characteristics. In addition, several other characteristics were measured, such as the reflectivity of the mirrors, resonance conditions, and their resonant behavior.

All actuation for this device is electrostatic, meaning force is generated by an electric field between differently charged electrodes. For the actuation of the focal control of the mirror curvature is induced by grounding the electrode connected to the mirror frame and charging the surface of the mirror with a positive DC voltage. A cross-sectional diagram showing this actuation setup is shown in figure 4.11. The electric field produced is concentrated in the small cavity under the mirror membrane. The small gap (less than 5 micrometers) between these electrodes allows a small applied voltage to generate the large electric field necessary to bend the membrane. While the reduction in the depth of this cavity decreases the voltage needed for actuation it also limits the maximum membrane deflection. This relates to the minimum achievable radius of curvature and minimum focal length, according to:

$$f = \frac{ROC}{2} = \frac{1}{2}\frac{\left(D_m/2\right)^2 + d^2}{2d} \qquad \text{(Eq. 4.1)}$$

Where f is the focal length of, ROC is the radius of curvature, and D_m is the diameter of the mirror, and d is the deflection at the center of the mirror.

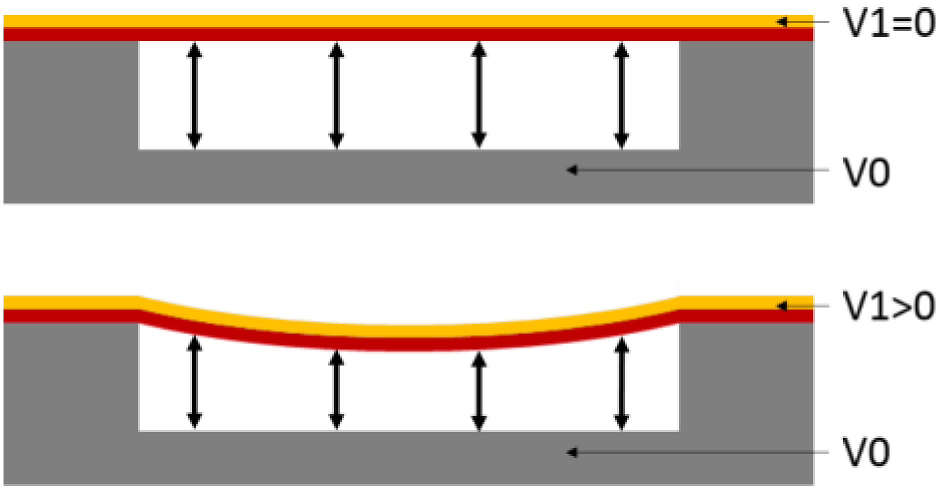

Fig 4.11: Membrane curvature is controlled with an electric field beween the gold reflective layer and the underlying silicon. The membrane is flat with 0 volts applied (top) and curved when a non-zero voltage is applied (bottom).

The measurement of the mirror deflection and curvature is done with a Veeco HD 3300 optical surface profiler. This optical surface profiler allows accurate mapping of the surface height without the risk of the device being damaged and while the mirror is under various actuation conditions. With this data showing the membrane deflection, the radius of curvature of the membrane and the focal length of the mirror can be calculated. Tuning of the focal length of the micromirror from infinite, (flat surface) with no applied voltage, to under 25mm, with less than 100 V applied (fig. 4.12 and 4.13).

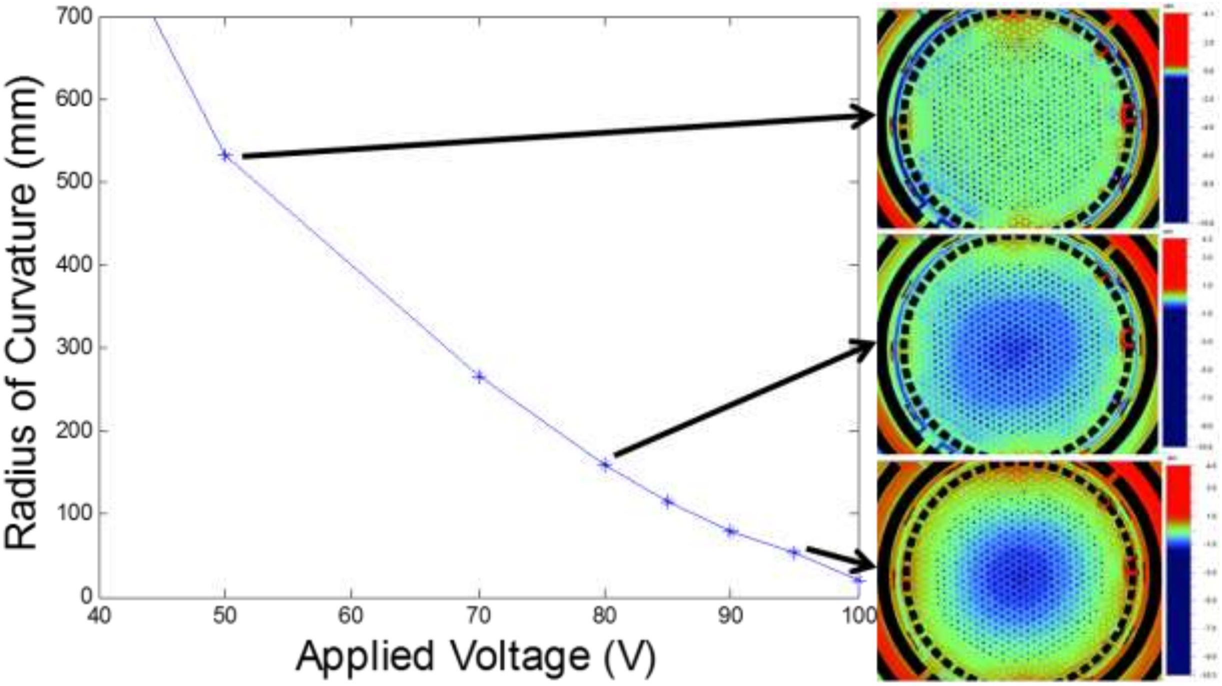

Fig 4.12: Radius of curvature versus the applied voltage for the micromirror device with corresponding heat map showing the membrane surface height. [29]

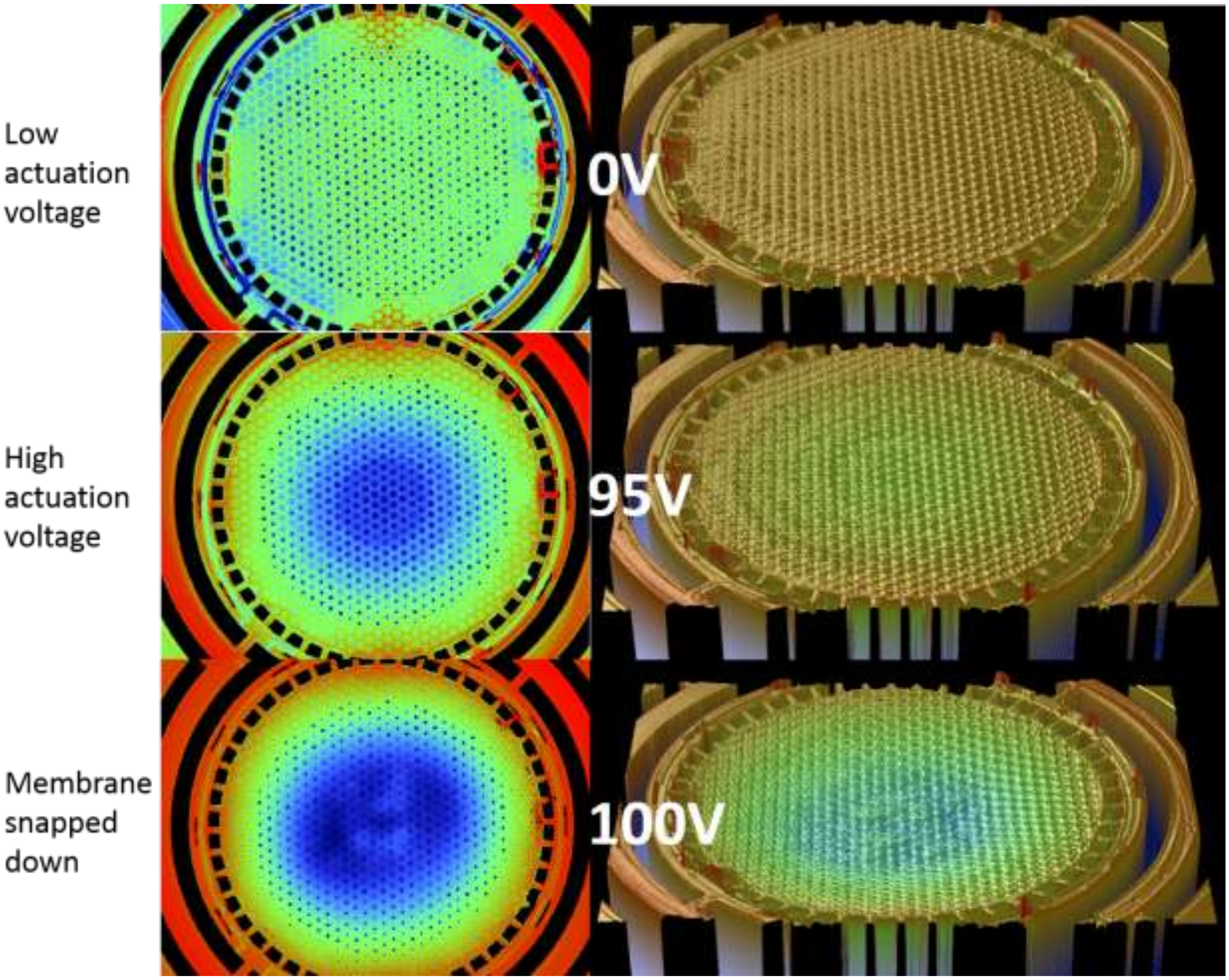

Fig 4.13: Heat maps corresponding to the height of the mirror surface (left) with 3-dimensional optical surface profiler images (right) for the mirror membrane with 0 volts (top) and 95 volts (middle) applied, and the membrane snapped down with 100 volts applied (bottom).

Focal control was also measured with a Newport LBP-3-USB beam profiler to view the cross-sectional intensity of the beam with varying actuation. As seen in figure 4.14, the beam comes into focus and then passes the focal point with an increasing voltage between 70 V and 90 V. Also important, for an imaging system of this type, is the beam shape. The beam as it exits the optical fiber has an intensity distribution that is highly Gaussian. With a perfect mirror profile it is possible to preserve this beam shape, however real mirrors are not perfect and always introduce some amount of distortion to the beam. To analyze the quality of the mirror surface, the intensity distribution of the reflected beam was measured. Under most actuation conditions, the correlation of the intensity profile of the reflected beam and the perfect Gaussian profile was greater than 90%. Figure 4.15 shows one intensity profile of the reflected beam with a 95% correlation with 87V applied to the micromirror.

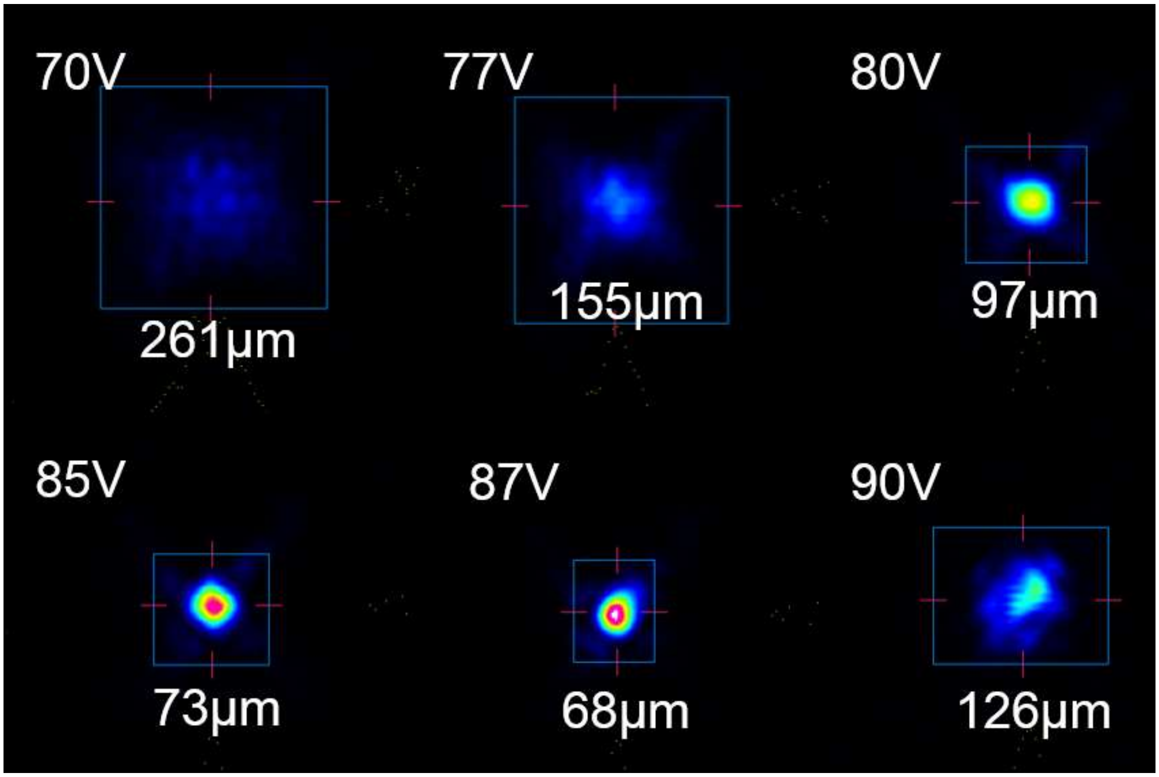

Fig 4.14: Cross-sectional image of the optical with color representing intensity. The beam passes through the focal point with a voltage from 70 V to 90 V.

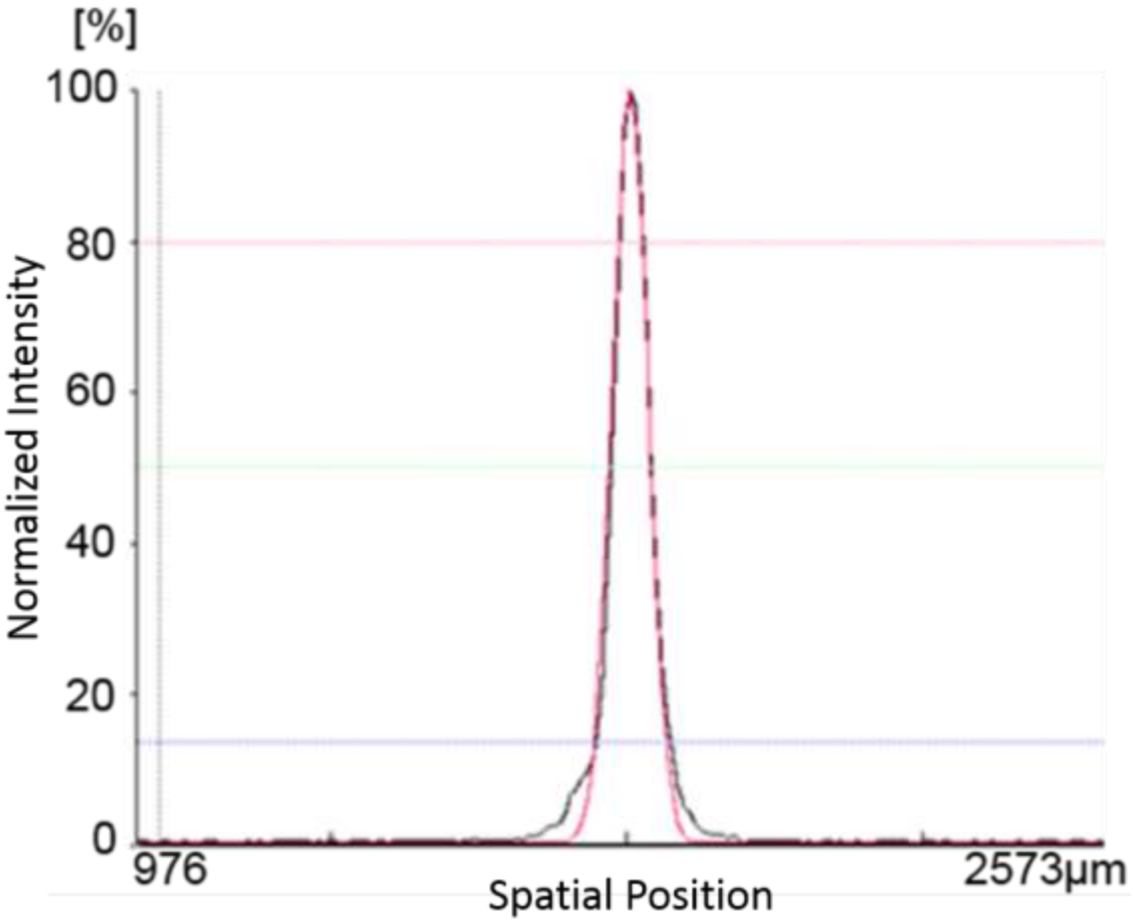

Fig 4.15: Intensity profile of the reflected optical beam (black) compared to an ideal Gaussian profile (red). The correlation of these two curves is greater than 95% with 87V applied to the mirror. The full-width-half-maximum (FWHM) of the focused spot is 68µm. [29]

To test the scanning performance of the mirrors, the silicon frame electrode used in curvature control along with the 4 electrodes patterned on raised pillars on a second wafer are needed for actuation. Each of these electrodes allows tilting of the mirror in a different direction allowing full 2-dimensional control of the mirror. The scanning of each mirror is characterized with static applied voltages and AC voltages tuned to the mechanical resonant frequency of the device. Due to the large electric field necessary to actuate the mirror, an amplifier must be used that is capable of generating high voltages. In this case, a Trek 2205 high voltage amplifier was used to generate the actuation voltage. For DC actuation the static voltage is simply applied to the two electrodes (fig 4.16). Alternatively, during AC actuation the mirror electrode is charged with a DC bias and a sinusoidal AC signal is applied to one or more of the underlying electrodes. The DC bias allows a larger electric field to be generated with the same magnitude AC signal.

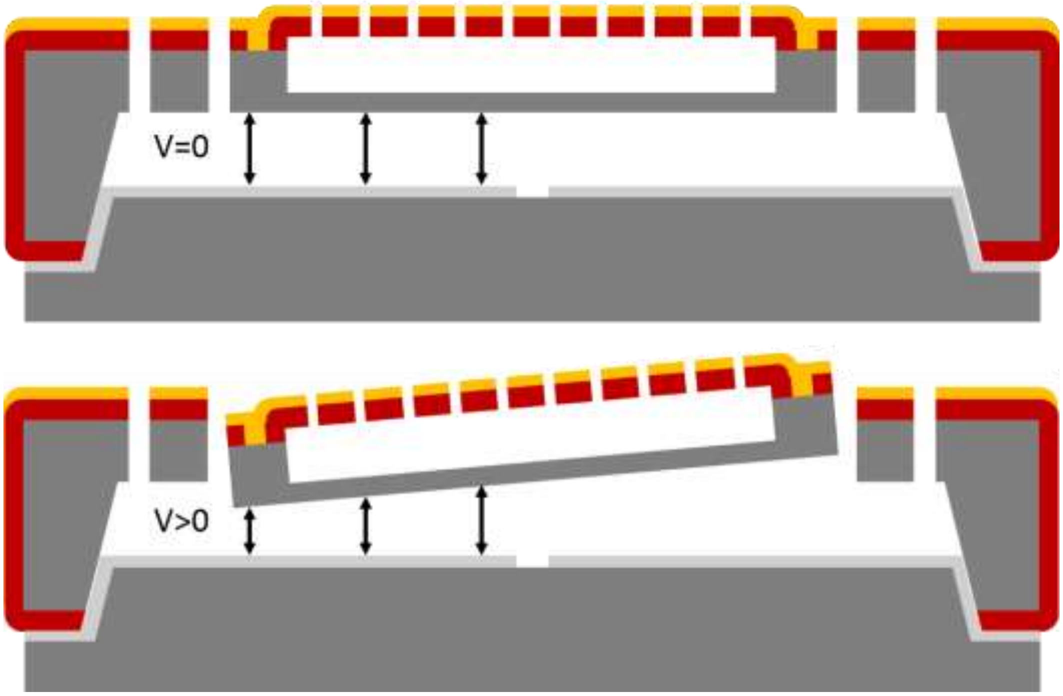

Fig 4.16: Mirror tilt is controlled with an electric field between the conductive silicon frame and the electrodes positioned beneath the mirror. With 0 V applied the mirror is flat (top) but begins to tilt when a voltage is applied (bottom).

As expected, the DC voltage needed to actuate the mirror is much greater than that needed for scanning at resonance. Additionally, the curve of deflection vs. voltage for the mirror at resonance is highly linear (fig 4.17(b)), while the curve with static actuation is very non-linear (fig 4.17(a)). The DC bias on the mirror when scanning at resonance is 60 V.

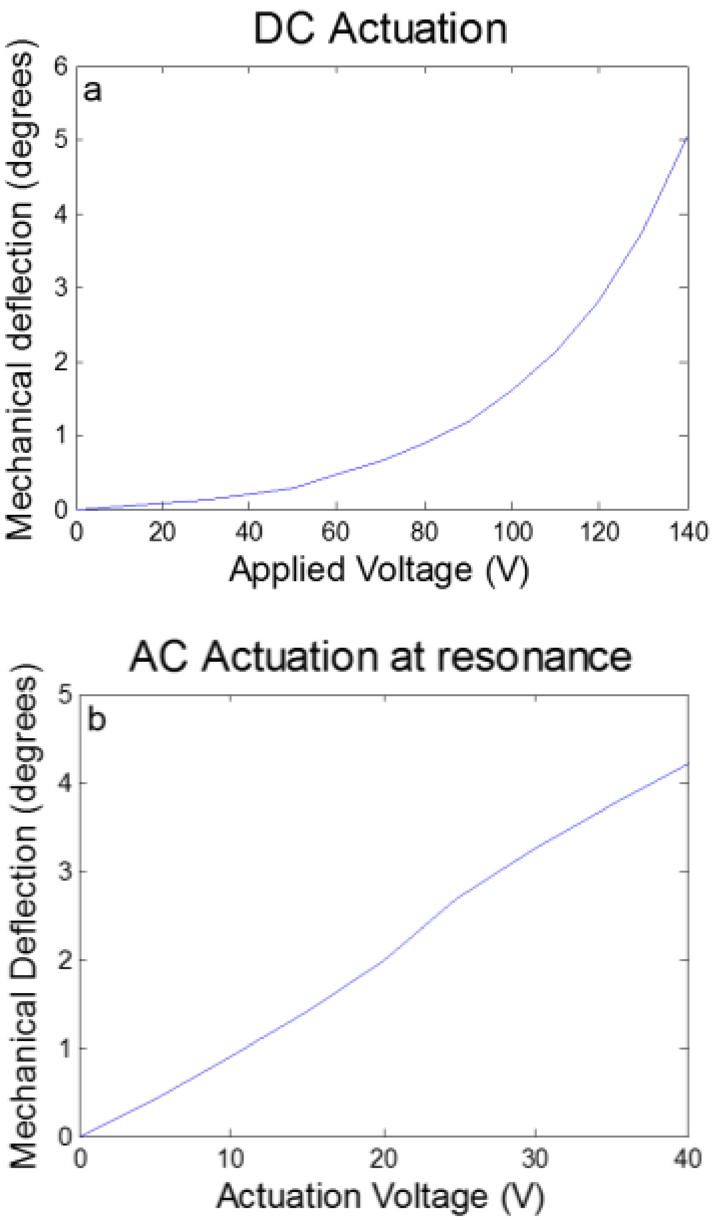

Fig 4.17: Mechanical deflection vs. voltage curves for the MEMS micromirror actuated at DC (a) and at resonance with a 60 V DC bias (b). [29]

The non-linearity of the mirror deflection with static actuation was expected due to the dependence of the electrostatic torque generated on the capacitance of the device. This capacitance changes with the spacing between the electrodes and as the tilt of the mirror increases this gap decreases increasing the electrostatic torque applied to the mirror. Because the mechanical torque generated by the torsion beams increases linearly with deflection the non-linear increase in capacitance is seen in the curve. The deflection of the mirror at resonance is not at equilibrium and therefore the non-linearity of the device capacitance does not affect the scan curve. Rather the deflection is governed by a balance in the energy being introduced to the system through actuation and the energy being dissipated due to mechanical damping. As shown in chapter 3 and seen in fig. 4.17(b), this results in a linear relationship.

To characterize the frequency response of the devices, voltage is applied to the mirror in the same manner as the resonant testing. While the magnitude of the mirror's deflection is measured the frequency of the signal is varied to produce a curve of mirror deflection vs. frequency (fig. 4.18).

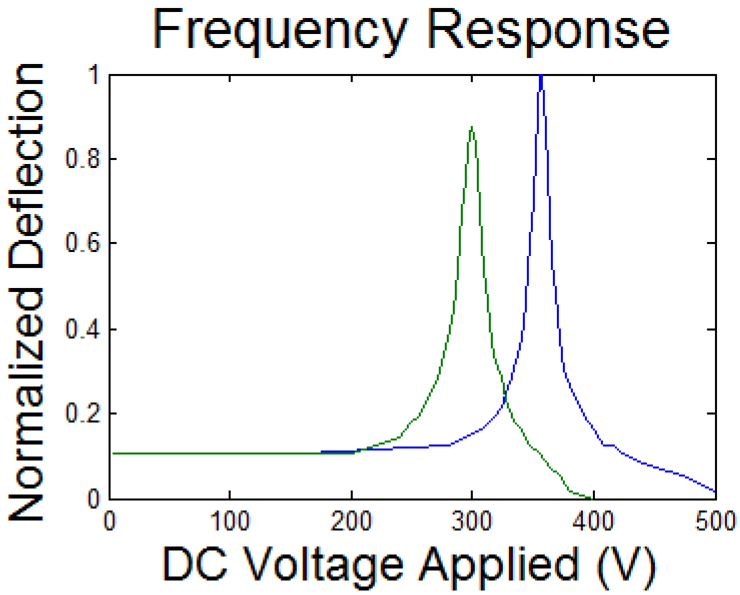

Fig 4.18: Frequency response of the MEMS micromirror showing the major resonant peaks for the inner axis (blue) at 357 Hz and outer axis (green) at 300 Hz.

4.3: Discussion

The dynamic performance of the micromirror devices met the specifications laid out in the design of the device. A maximum optical scan angle of greater than 20 degrees was achieved. Additionally, very good controllability of the mirror curvature was demonstrated. Tuning of the focal length between infinite and 25mm was achieved with a 100V actuation signal. With several devices fabricated we have also shown that this device can be customized to suit a specific application. By tuning the torsion beam geometry devices can be made to have lower actuation voltages or higher scanning frequencies. The characteristics of the focal length tunability can be modified by changing the nitride layer thickness, the number of tethers around the mirror, or by increasing or decreasing the depth of the cavity beneath the mirror membrane. Increasing this cavity depth increases the maximum deflection which lowers the minimum focal length that can be achieved but also increases the necessary actuation voltage. While the non-linear scanning characteristics of the mirror (with respect to voltage for DC actuation and with respect to time for resonant actuation) necessitates calibration before imaging. The reliability of the mirrors makes the calibration fairly accurate.

Chapter 5: MEMS Micromirrors for Spectral Domain OCT

5.1: Device Design and Fabrication

In addition to our primary application with time domain OCT, devices were fabricated for use with a spectral domain OCT system. For this application different device specifications were needed. For time domain OCT, each depth data point is generated by sampling the data as the depth is scanned. For spectral domain OCT, all of the depth data is obtained simultaneously. Hence, control of the mirror curvature is unnecessary. Secondly, much higher optical reflectivity was required. For the 3-dimensional devices the released membrane needed for focal controllability necessitated periodic etch vias in the surface of the mirror. While allowing the complete release of the membrane these vias also degraded the optical performance of the mirror by increasing the diffraction off the membrane. Modifying the mirror to not include focal tunability, the diffraction causing vias become unnecessary. This requires the device to be redesigned, including complete removal of the silicon nitride before metal deposition and a material change for the torsion springs.

In most optical applications the flatness of a surface is important because any roughness or curvature distorts the reflected beam. This is true for our devices. The main cause of intrinsic curvature in our devices is film stress between the LPCVD deposited silicon nitride and the silicon. Therefore, the removal of the nitride layer from the final device structure is imperative. Without silicon nitride as the tether material, the layer that is best suited to act as torsion springs is silicon. In silicon the fabrication process requires the tether to be the same thickness as the mirror plate. With the same spring tether design and much thicker silicon as the mechanical material, the spring constant of the devices would be several orders of magnitude higher. This would require a similar increase in actuation voltage to achieve scanning. To reduce this to a more practical value, the geometry of the spring must be altered. The reduction in spring stiffness was achieved through the use of a serpentine structure [32]. Figure 5.1 displays an optical micrograph of the fabricated serpentine structures with the length, width and thickness of the fingers being 150 µm, 5 µm, and 20 µm respectively. These serpentine springs were designed to have roughly the same spring constants as the previous silicon nitride tethers.

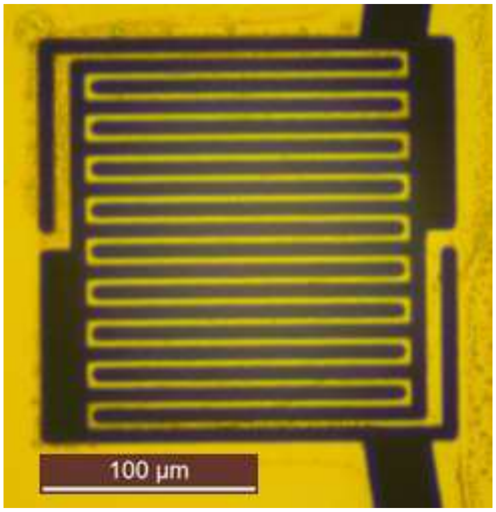

Fig 5.1: Optical microscope image of a silicon serpentine tether.

The updated tether designs necessitated several important changes in the fabrication process, including the substrate and the release of the device. Because the updated springs are silicon, final release of the device in KOH, as in previous designs, would also destroy the serpentine tethers. Instead, DRIE was used in place of the KOH release. The Bosch etching process [33], that is used in most DRIE etching systems, alternates between an etch step and a deposition step. While allowing very high aspect features to be created this etch process also creates a large amount of heat. This heat causes issues with the final release of the micromirrors.

When the mirror is released from the substrate, the only path for heat dissipation from the mirror plate is through the thin serpentine tethers. This large heat gradient commonly destroys the tethers, and therefore, the devices. To allow full release of the device without causing damage, a silicon-on-insulator (SOI) wafer with an underlying sacrificial silicon oxide layer was used for the fabrication of micromirror devices for spectral-domain OCT. While also allowing more consistent device thicknesses, this allows heat generated in the DRIE etch to be dissipated through the sacrificial layer before full release in a wet etchant.

The fabrication process starts with deposition of a PECVD silicon nitride etch mask (300 nm thick) on both sides of the SOI wafer (fig. 5.2(b)). KOH is used to etch through the silicon handle wafer to the buried silicon oxide layer (fig. 5.2(c)). The silicon nitride is then removed using 85% phosphoric acid at 160°C. A thin Au layer (75 nm) is deposited on the surface with a very thin Cr adhesion layer (fig 5.2(d)). The thickness of the metal layers was minimized to reduce the stress between the films. The metals are patterned using a wet chemical process before DRIE defines trenches through the device layer (fig. 5.2(e)). Final release of the device is completed in HF to remove the silicon oxide from the device (fig. 5.2(f)).

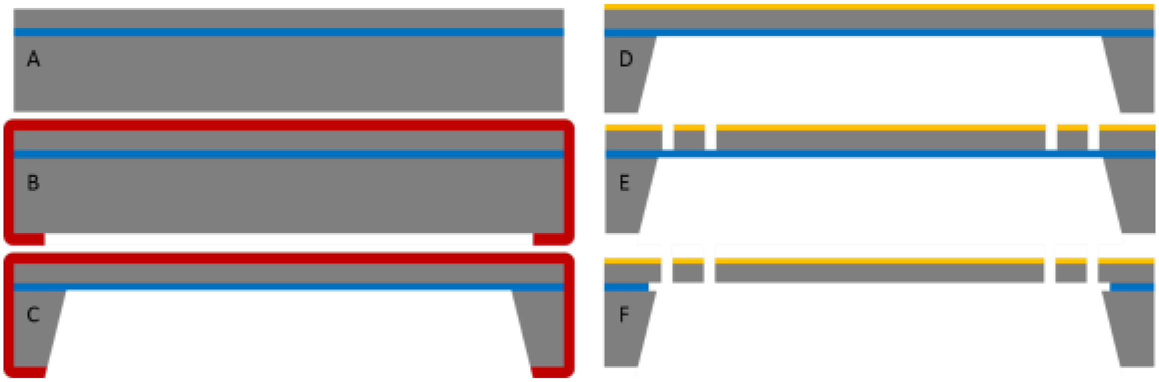

Fig 5.2: (A) A double side polished silicon on insulator (SOI) wafer (B) PECVD is used to deposit a conformal silicon nitride on both sides of the wafer and the backside is patterned (C) The backside of the wafer is etched with KOH to the silicon oxide layer in the location of the mirrors (D)

Phosphoric acid at 160°C is used to remove the silicon nitride (E) The metals are etched before trenches are etched into the silicon (F) HF is used to finish the release of the device.

5.2: Device Testing and Discussion

These scanning devices were tested in the same way as the scanning aspect of the 3-dimensional devices. A voltage is applied to underlying metal electrodes while the silicon mirror plate is held at ground. As observed previously, the DC actuated curve is non-linear (fig. 5.3(a)) and the resonant curve is highly linear (fig. 5.3(b)). The resonant curve was obtained with a 60 V DC bias.

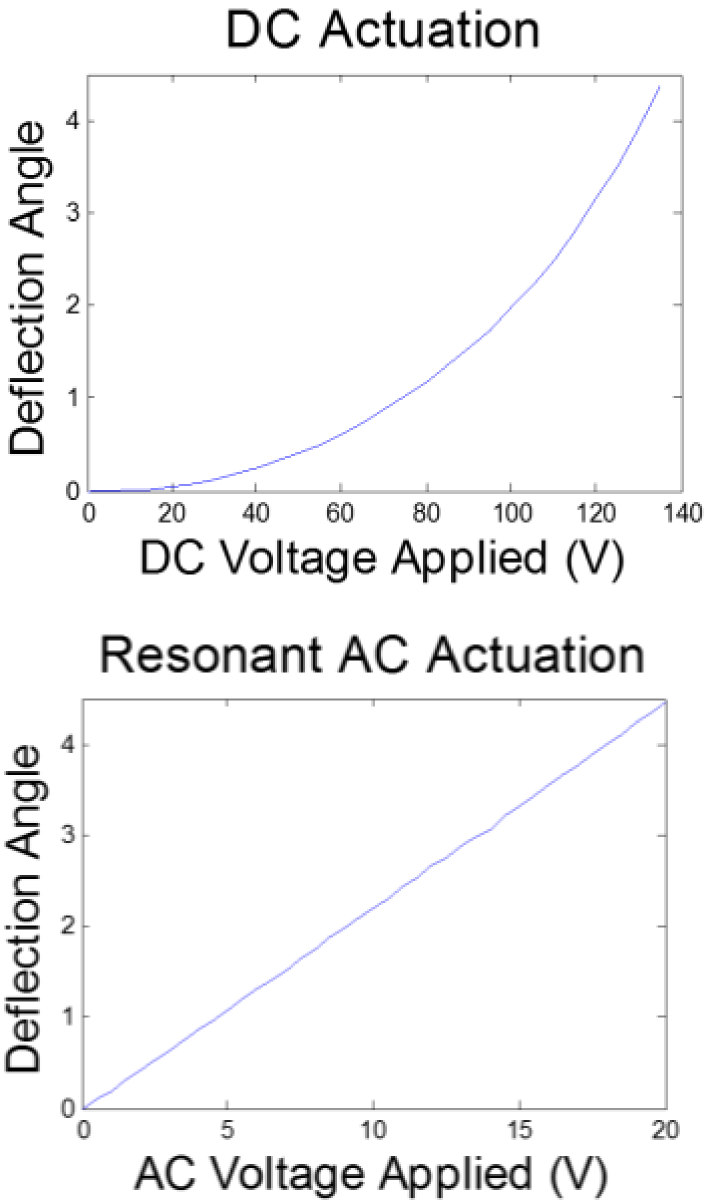

Fig 5.3: MEMS micromirror mechanical deflection vs. applied voltage at DC and (top) at the mechanical resonant frequency with a 60V DC bias (bottom).

The frequency response of these devices was characterized by varying the frequency of the voltage signal applied to the electrodes while monitoring the deflection of the mirror. Figure 5.4 shows the frequency response of the mirror deflection.

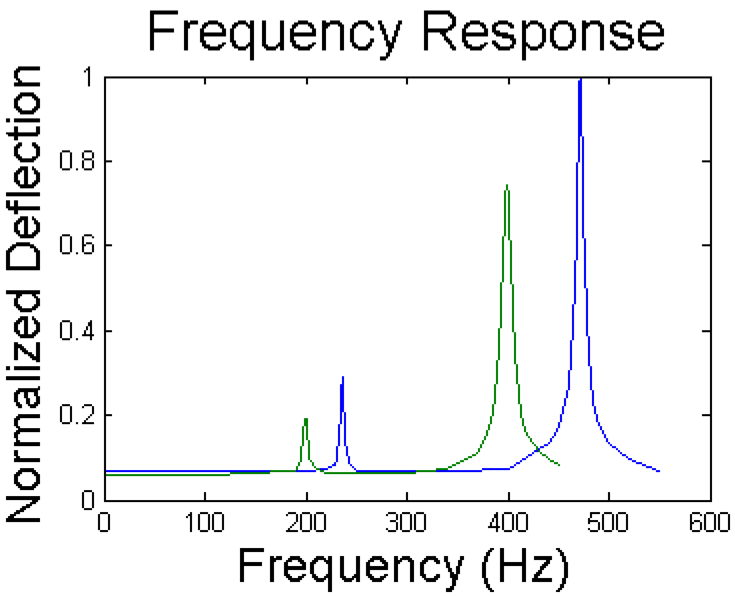

Fig 5.4: Frequency response of the micromirror showing the major resonant peaks for the inner axis (blue) at 472Hz and outer axis (green) at 399Hz.

These curves show the main resonant peak for the outer axis at 399 Hz and at 472 Hz for the inner axis. Also visible on these curves is a minor peak at half the main resonance peak frequency. The figure displays the magnitude of the mirror deflection corresponding to an applied voltage signal at the x-axis frequency. Therefore, the mechanical oscillation is not necessarily matched to the frequency of the applied signal. These minor resonance peaks correspond to mechanical oscillations at the frequency of the main resonance excited by the second order harmonic of the actuation waveform.

The scanning performance of these mirrors is very similar to the 3-dimensional device with a large achievable scanning range and linear resonant behavior. Removal of the etch vias, however, allows for a significant improvement in reflectance. A reflectivity of greater than 98% has been measured for these devices. This high reflectivity allows the use of these devices in a spectral domain OCT system.

Chapter 6: OCT Imaging

OCT imaging is an interesting method for tissue analysis in disease diagnostics. There are two main classifications of OCT systems: time-domain and frequency-domain OCT systems. The micromirror devices introduced in the previous chapters were integrated into a bench-top OCT setup for imaging of multi-layer structures to demonstrate both the spatial and depth resolution provided. Imaging results for both time-domain and frequency-domain OCT setups, obtained with both device structures are presented in this chapter.

6.1: Time-Domain OCT Testing

6.1.1: Time-Domain OCT System Operation

The MEMS micromirror devices were designed for use in a time-domain OCT system. As described previously in chapter 2, a time-domain OCT imaging system utilizes a low-coherence light in a Michelson type interferometer. Dynamic control of the length of the reference arm is used to control the depth of the scan. With the system measuring the interference signal between the two optical paths, as the path length of the reference arm is scanned, data can be acquired corresponding to various depths in the sample of interest. The scanning MEMS micromirror is positioned in the sample arm to scan the beam in the two lateral directions of the image. The dynamic focal control of the mirror allows the depth of focus to be matched to the path length as the length of the reference arm is scanned, providing consistent spatial resolution throughout the image.

In the time-domain OCT system specifically built for testing of the MEMS devices, a fiber-coupled superluminescent diode centered around 1325 nm provides low-coherence light for the imaging system. The FWHM of the broad-band light source is ~100 nm. Hence, the coherence length corresponding to the axial resolution of the depth imaging can be calculated.

$$L = \frac{2\ln(2)}{\pi n}\frac{\lambda^2}{\Delta\lambda} = \frac{.4413}{n}\frac{1325^2}{100} = \frac{7.748\mu m}{n} \qquad \text{(Eq. 6.1)}$$

In air (n=~1), the depth resolution of the imaging system is expected to be ~7.7 µm. The resolution in tissue will be smaller because of the larger refractive index.

The light is split between the two beam interferometer paths by a 50/50 fiber coupler. The reference arm utilizes a rapid-scanning optical delay line (RSOD) for control of the path length [34]. This setup employs a galvanometer mirror as the method of path length control. The light is transferred to the free space optical setup through a fiber collimator. The 2-pass RSOD optical setup is shown in fig 6.1.

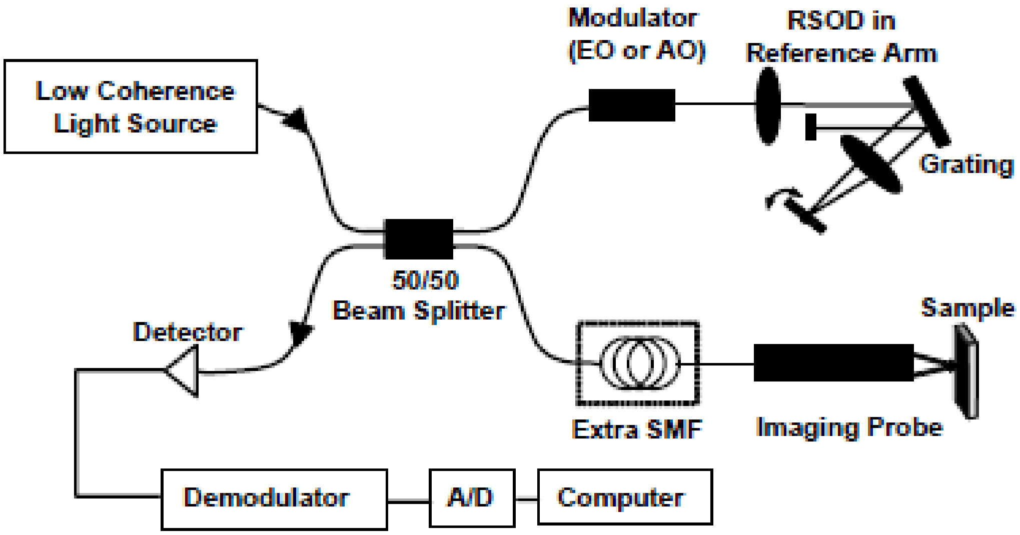

Fig 6.1: Optical setup for the time-domain OCT system including the RSOD and sample arm. After the light is split by the 50/50 beam splitter (in our case a fiber coupler), the light reflected from the reference mirror and the sample returns to the beam splitter and interferes. The output light is detected before being filtered, amplified and digitized. [34]

In this RSOD, rotational movement of a galvanometer mounted mirror provides the control of the optical path length. The path length change is dependent on the deflection angle of the mirror. This is shown in more detail in figure 6.2.

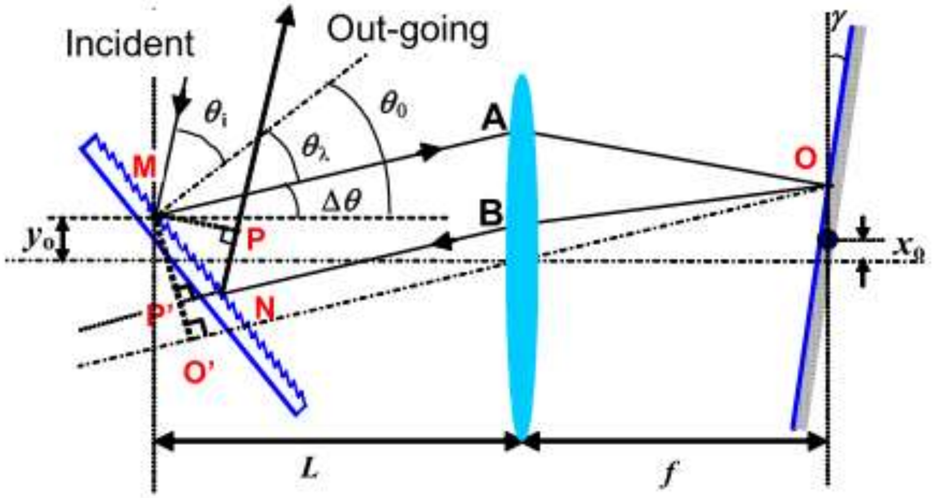

Fig 6.2: Detailed diagram showing the path length change in the RSOD. [34]

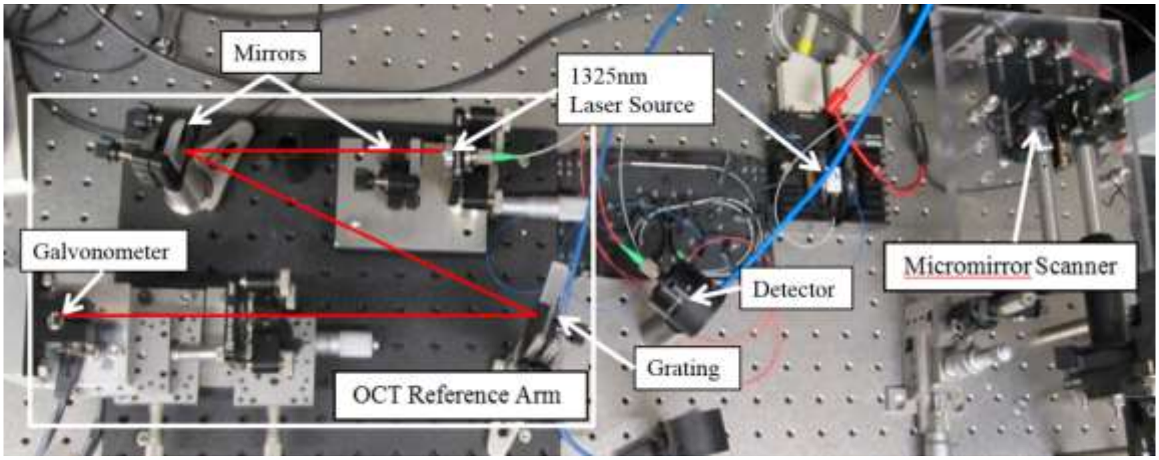

Fig 6.3: Optical image of the time-domain OCT setup showing the RSOD reference arm and the micromirror scanner. The red line shows the optical path in the RSOD.

6.1.2: Time-Domain OCT Imaging

In order to image using this system the light must be focused for the beam to be confined to the mirror area before being focused on the sample. In the free space optical setup this is achieved with several focusing lenses. A fiber collimator containing a fiber mount and a collimating lens is mounted to the optical bench. The light is directed onto the micromirror and then focused on the sample using a high NA lens. The light reflected or scattered from the sample travels back on the same path and is recollected by the fiber.

The scanning capabilities of the MEMS micromirror determines the quality of the image acquisition. The spatial location of the beam on the sample is determined by the scan angle of the micromirror. In order to achieve a distortionless image, there must be a regular spatial distribution of acquired points. This corresponds to 2-dimensional linear scanning of the mirror. This is difficult because of the non-linear characteristic of the micromirror's scanning. With static actuation, the scanning is non-linear with respect to voltage due to the capacitance change of the device (Eq. 3.4). This distortion can be seen in fig. 6.4 below. While at resonance, there is a linear relationship between voltage applied and deflection angle. The spatial scanning of the mirror at resonance, however, is non-linear with respect to time. Therefore, in order to get non-distorted images, either the voltage curve applied to the mirror must be calibrated or post processing of the raw data must be performed to extract the desired image data. To allow for accurate processing, the return intensity must be sampled at a frequency several times higher than the pixel rate. The maximum data acquisition rate for the analog to digital converter used in the system was 92kS/s. This limits the maximum resolution of the image in one direction.

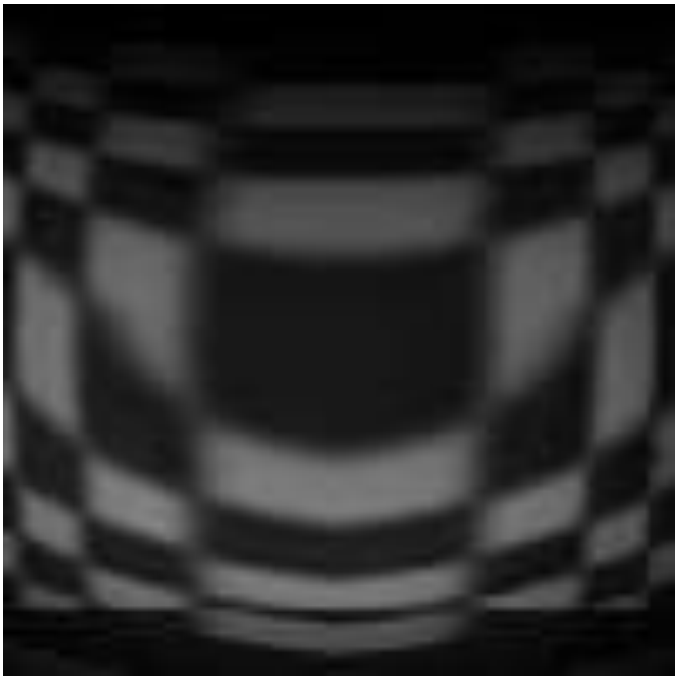

Fig 6.4: The non-linear behavior of the device capacitance causes non-uniform spatial scanning. This distorted image was obtained with the MEMS micromirror before voltage waveform calibration.

The calibration of the voltage waveform can be achieved in several ways. The simplest method, perhaps, is the application of the inverted deflection vs. voltage curve. For this method, deflection data is taken with a dense range of voltages giving a highly sampled curve of deflection angle versus voltage. This data is inverted by swapping the x and the y axes and a curve is fit. This fitted curve can then be used to actuate the mirror with linear spatial deflection. This method was used with some success, but while it accounts for device capacitance change in one direction it neglects the difference in device capacitance when high voltages are applied to both axes. In order to account for the 2-dimensional capacitance variations, a 2-dimesional calibration method must be used.

The method chosen to achieve the desired calibration results was a 2-dimensional interpolation algorithm. A two-dimensional array of voltages corresponding to the x and y axes is applied to the mirror. The spatial location of the focused laser spot is measured with a beam profiler and recorded. This data is fed into the algorithm and cubic interpolation is used to calculate the necessary voltages for each axis to drive the mirror to these points. Because interpolation is only an estimate of the real function, it has some error, and therefore the algorithm performs better with denser original data.

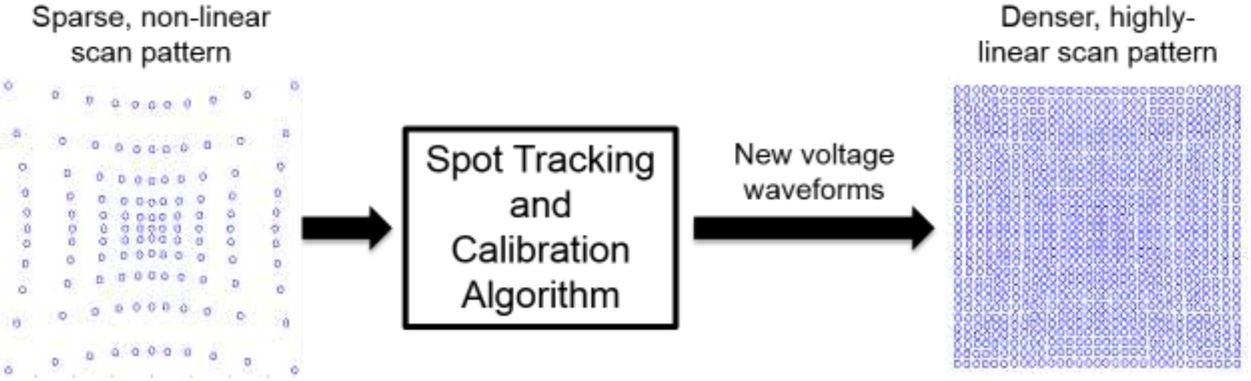

Fig 6.5: The initial spatially non-uniform data with 2 actuation voltages and 2-dimensional position data is input into the interpolation algorithm. The output is a densely spaced, highly linear scan pattern with the corresponding actuation voltages.

Using this method of mirror calibration, the non-linear behavior of the mirrors can be corrected to a highly uniform pixel distribution. In order to test the micromirror scanner, imaging samples were prepared. These test samples were fabricated by sputter depositing a layer of aluminum on a silicon wafer and patterning this aluminum with photolithography and a wet chemical etch step. Various sizes of checkerboard pattern, ranging from 3 µm and 200 µm and other structures of similar sizes were fabricated.

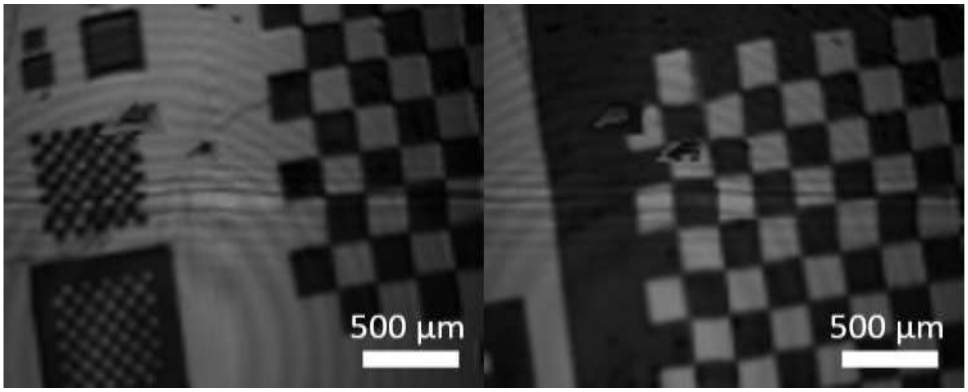

Fig 6.6: 2-dimensional spatial images of the fabricated test structures using the time-domain OCT system. The left image includes 50 µm checkerboard patterns (lower left) and part of the 200 µm checkerboard pattern (upper right). The right image shows the 200 µm checkerboard pattern.

Images displayed in fig. 6.6 demonstrate good linear spatial control of the focused beam spot. The major defect in the image is the horizontal distortion through the center of each of the images. This distortion is caused by the non-linear behavior, around 0 V, of the voltage rectifier used to generate the actuation signals. Through the use of a four output digital-to-analog converter, the necessary output signals can be generated without the need for rectification, removing the distortion. To analyze the resolution of the imaging system, images were taken of various sizes of checkerboard patterns.

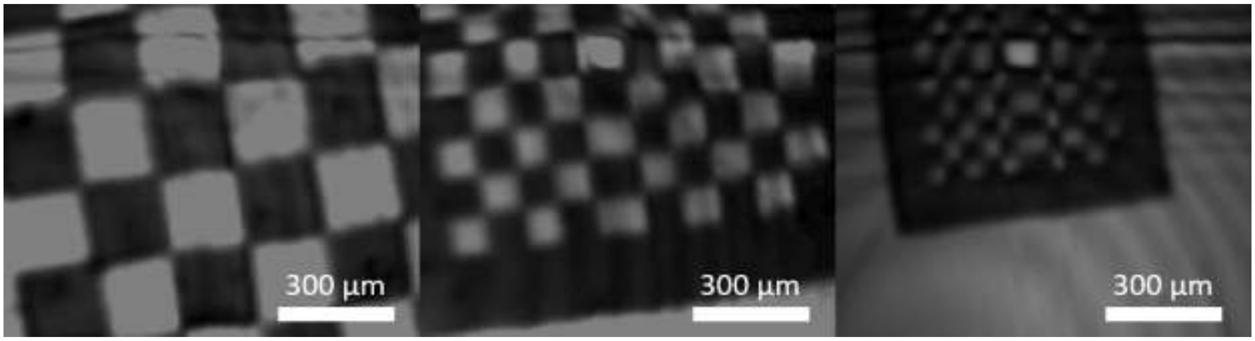

Fig 6.7: 2-dimensional spatial images of checkerboard patterns with 200 µm squares (left), 100 µm squares (center) and 50 µm squares (right).

The images displayed in fig. 6.7 demonstrate that the system is able to resolve 50 µm features. Through imaging and measurement of the size of the focused beam the estimated spatial resolution of the system is ~30 µm.

With the successful demonstration of spatial imaging in the time-domain OCT system, cross-sectional imaging is necessary to prove the 3-dimensional imaging capability of the system. Cross-sectional images were obtained for several samples starting with the reflective aluminum on silicon checkerboard patterns used in the spatial scanning (fig. 6.8).

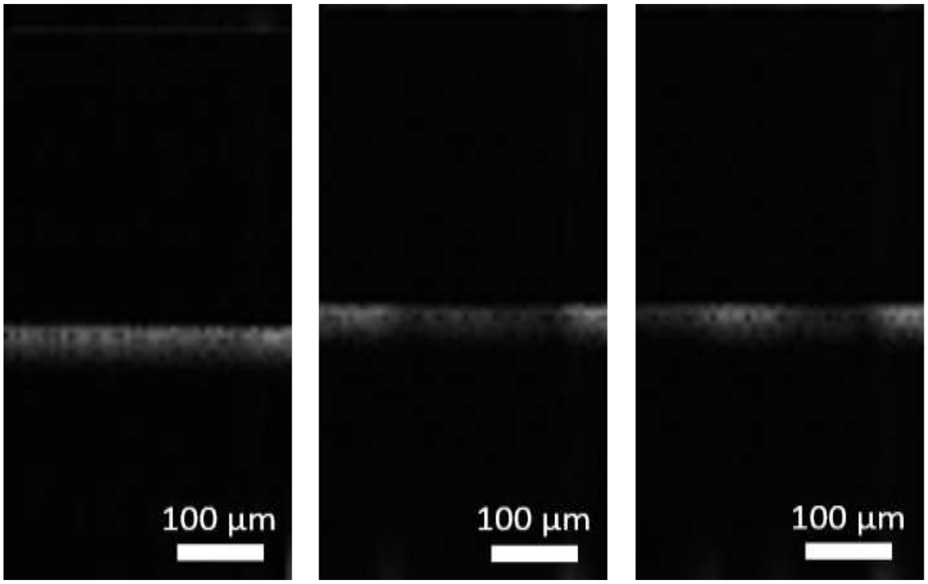

Fig 6.8: 2-dimensional cross-sectional images of an aluminum mirror (left) and checkerboard patterns with 200 µm squares (center) and 100 µm squares (right).

In fig. 6.8 the surface of the test structure is clearly visible with an intensity difference between the periodic aluminum and silicon pattern. While this allows the system to be calibrated, to truly test the system more complicated structures were required. For our testing, an offset stack of microscope cover glass slides were used. The position of each was slightly offset from the next, producing a stair step structure. Figure 6.9 displays the time-domain OCT images obtained for this test structure.

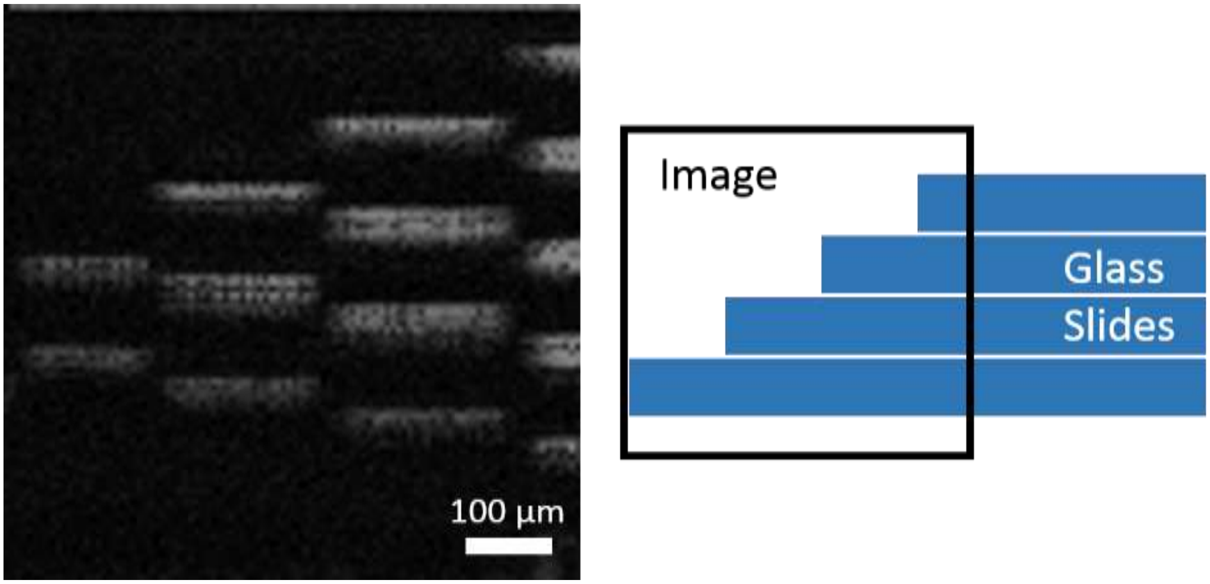

Fig 6.9: A 2-dimensional cross-sectional image of an offset stack of microscope cover glasses (left) with a corresponding diagram showing the sample structure (right).

Each cover glass in fig 6.9 is 140 µm thick. At the non-surface boundaries double lines can be observed, caused by the air gap between the glass slides. The discontinuity of each glass slide across the images is caused by the refractive index difference between air and glass. Because the depth is determined by optical path length, the depth length in the image is proportional to the refractive index of the material. This causes the 140 µm glass slide to appear ~200 µm thick in the image.

6.2: Spectral Domain OCT Testing

6.2.1: Spectral-Domain OCT System Operation

As time-domain OCT, spectral domain OCT systems are designed to enable 3-dimensional imaging. The method of acquiring the depth information, however, differs from a time-domain system. In time-domain OCT depth of the scan is determined by the path length of the reference arm. This necessitates scanning the length of the reference arm to control the imaging depth. In a spectral domain OCT system, the length of the reference arm is fixed. The depth information is obtained through the analysis of the phase data of the different wavelengths of light contained in the signal. A spectrometer is constructed, composed of a diffraction grating and a linear detector array, to diffract the incoming light according to its wavelengths and measure the intensity of the different wavelengths of light contained in the spectrum. Unlike the time-domain system where the resolution was dependent on the optical source, the axial resolution in this type of system is related to the spatial resolution of the detector strip. A more precise measurement of the intensity spectrum will result in greater resolution for the depth imaging.

This spectral domain OCT system uses a broadband superluminescent diode, centered around 1300 nm with a bandwidth of 83 nm. The light from the laser is split equally between the two interferometer paths with a 2x2 fiber coupler. After the two signals interfere, the data is recorded by the spectrometer and the signal is digitized. A data processing algorithm is then used to create the 2-dimensional image from the digital data.

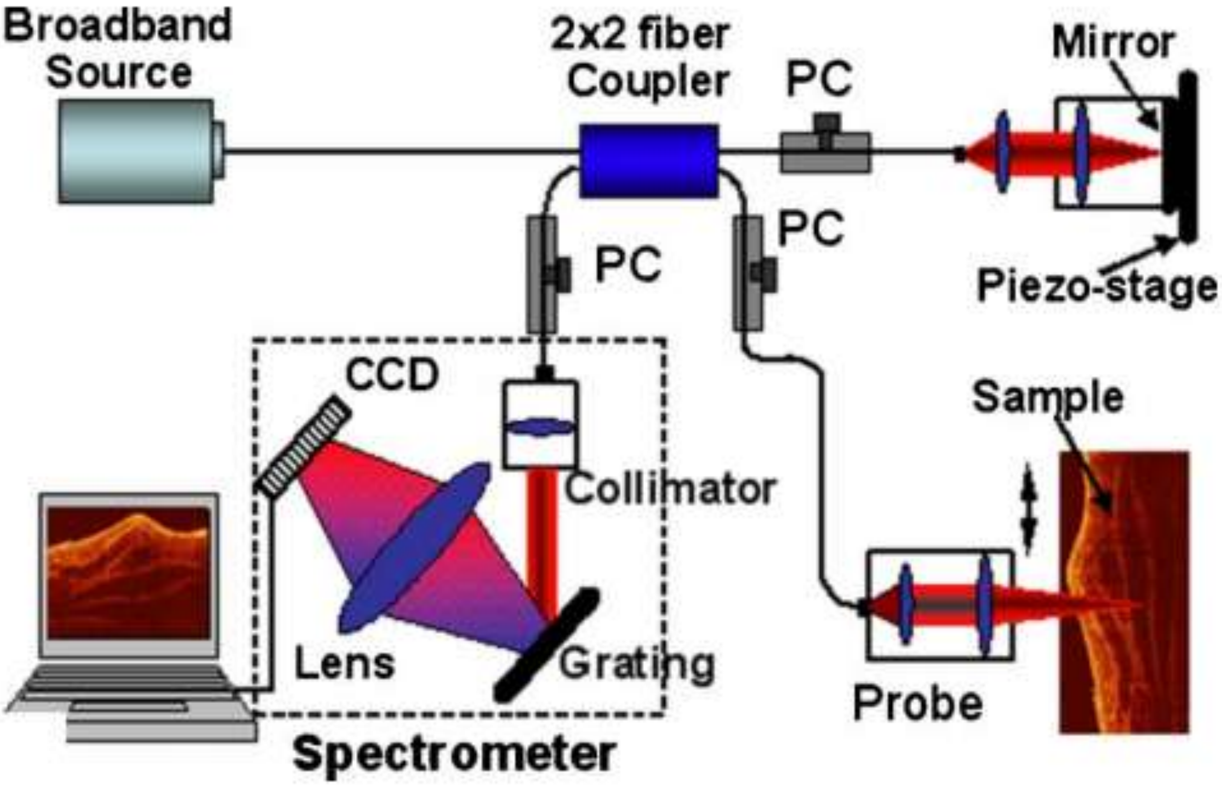

Fig 6.10: Schematic of the spectral domain OCT system. The light is split between the 2x2 fiber coupler. After reflection from the sample and reference mirror the light is interfered by the fiber coupler, and exits the fiber through a collimator. The light is then diffracted by a grating and measured and digitized. [23]

6.2.2: Spectral-Domain OCT Imaging

To test the performance of the MEMS devices in the spectral-domain OCT system several test samples were imaged. This allows testing of both the capability of the MEMS device in this system and overall system performance to ensure optimal operation. The first sample imaged was a sheet of white paper (fig 6.11). This is a good first sample because there is a large amount of scattering from the surface and there is a clear interface.

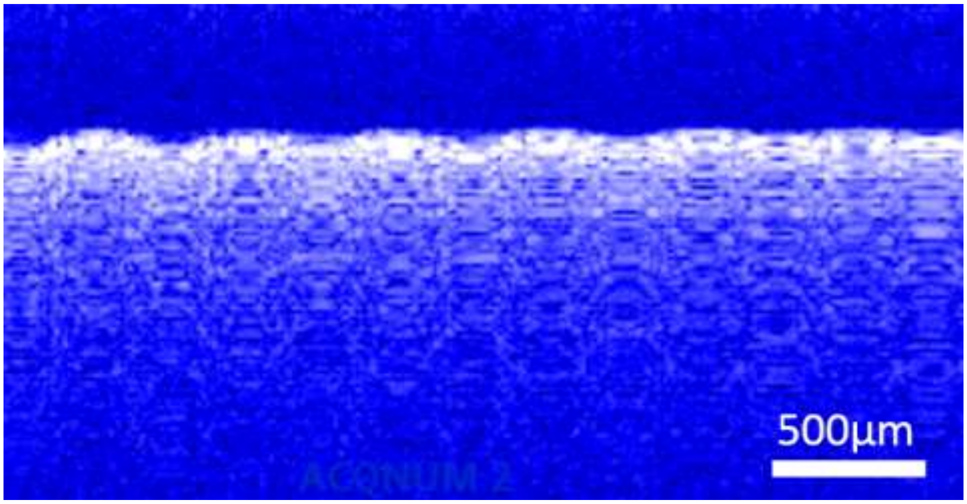

Fig 6.11: 2-dimensional cross-sectional image of a piece of white paper obtained with a spectral domain OCT system. The signal strength diminishes as the depth into the paper increases.

The surface of the paper is clearly visible in the picture as the bright white line across the top of the image. As the depth into the paper increases, the signal diminishes. In the image, this is shown by the brightness decrease of the picture in the vertical direction. Another test sample that is interesting to image is a layered transparent material (fig. 6.12).

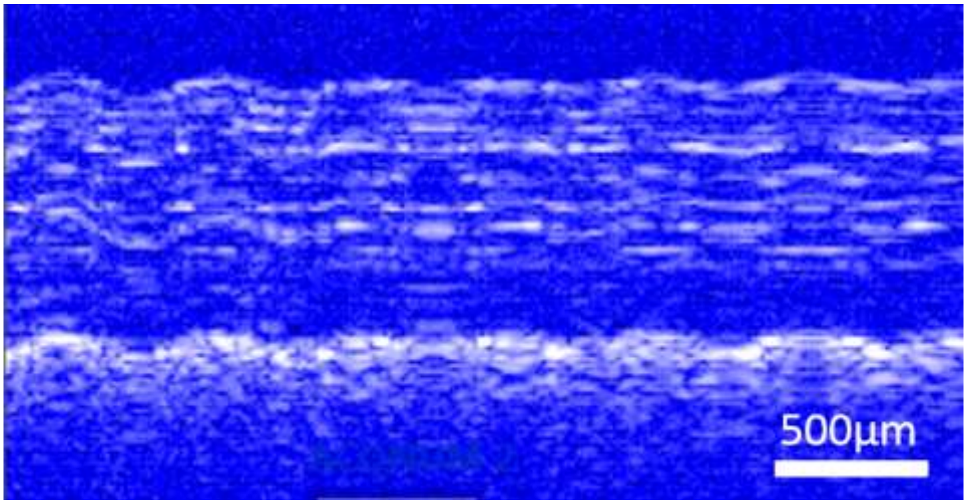

Fig 6.12: 2-dimensional cross-sectional image of a stack of transparent tape obtained with a spectral domain OCT system. This structure allows the depth imaging of the system to be tested. As with the image of paper, the signal strength diminishes as the depth increases. The strong signal towards the bottom of the image is the paper that the tape stack is mounted on.

The layered structure of the tape stack is visible in the image in fig. 6.12. The bright layer beneath the tape layers is the paper that the tape is mounted on. After imaging of test samples that allowed the calibration and optimization of the setup, imaging of tissue samples was achieved. For these tests the tissue sample was the ear of a mouse (fig.6.13).

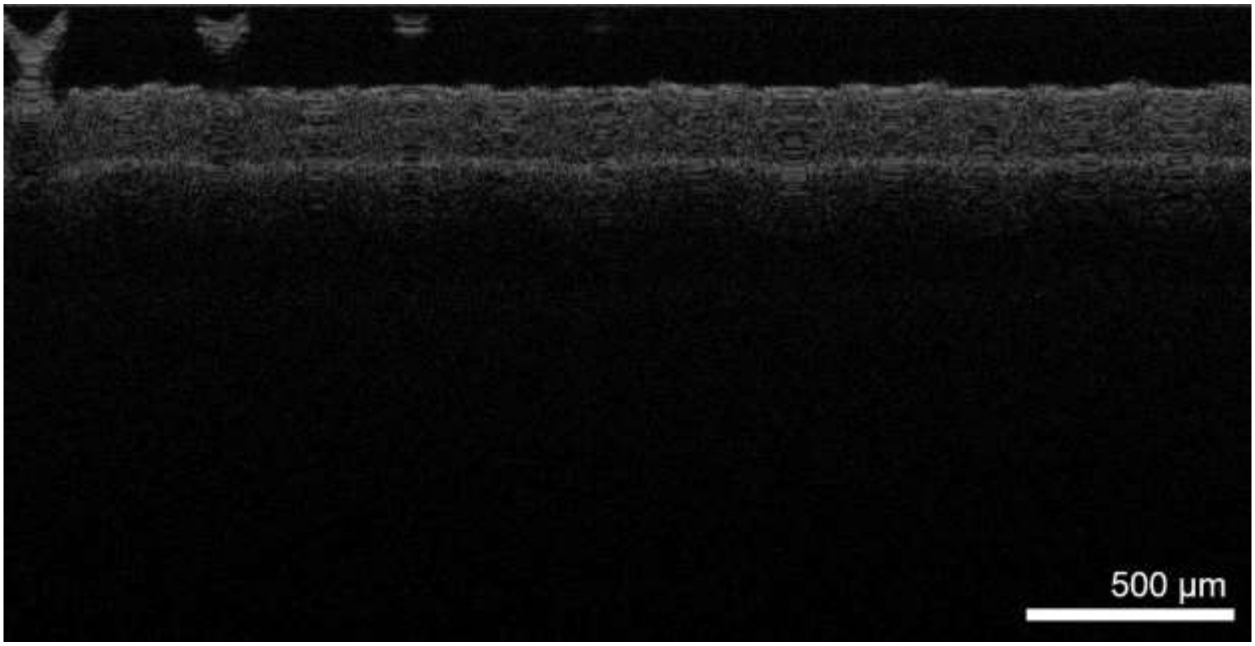

Fig 6.13: 2-dimensional cross-sectional image of a mouse ear. The surface of the ear is clearly visible towards the top of the image. The second layer seen below the surface is the cartilage inside the ear.

The cross-sectional image of a mouse ear displayed in fig. 6.13 successfully demonstrates the ability to image biological tissue. The first strong boundary near the top of the image corresponds to the surface of the ear. Deeper into the sample a second layer is visible. This layer is the cartilage inside the ear.

Chapter 7: Conclusions

MEMS micromirror devices for endoscopic imaging applications have been designed, fabricated and tested. Common microfabrication processes and readily available materials were utilized for a low-cost integration into future endoscopic imaging systems based on OCT. The devices integrate 2-dimesional scanning functionality with dynamic focus tracking, making them promising for *in-vivo* depth-resolved tissue analysis. The micromirrors provide a large scanning range, >20 degrees of optical scanning in both spatial directions, as well as a tunable focal length between infinity and 25 mm. These capabilities are achieved by electrostatic actuation of an 800 µm diameter mirror membrane, and with lower operating voltages compared to similar, previously reported devices [27]. Additionally, devices designed specifically for use in a spectral domain OCT system were tested and showed similar large scanning angle and low voltage actuation characteristics. Balancing the trade-off between spring constant and actuation voltage for devices of this design, fairly high mechanical resonant frequencies of up to 500 Hz were achieved. The comparatively high mechanical resonance frequency allows the angular position of the micromirror to be repositioned at a faster rate, and therefore increase the frame rate of the corresponding imaging system.

Successful imaging in both time-domain and spectral-domain optical coherence tomography systems has been demonstrated using these MEMS scanning micromirror devices. To achieve distortionless imaging, a calibration method was developed that allows linear, 2-dimensional control of the position of the focused laser spot. This enabled successful cross-sectional and spatial imaging using both spectral and time-domain OCT systems.

While this technology has proven successful for beam scanning and focus tracking in a time domain OCT system, the following steps remain before a viable clinical application can be approached. The first, and possibly most difficult, would be the optical packaging. The micromirror devices were designed to fit inside a probe small enough to be used in the working channel of a standard endoscope (less than 3 mm). Three potential packaging designs have been investigated, two for forward facing imaging and one for side facing imaging (fig. 7.1).

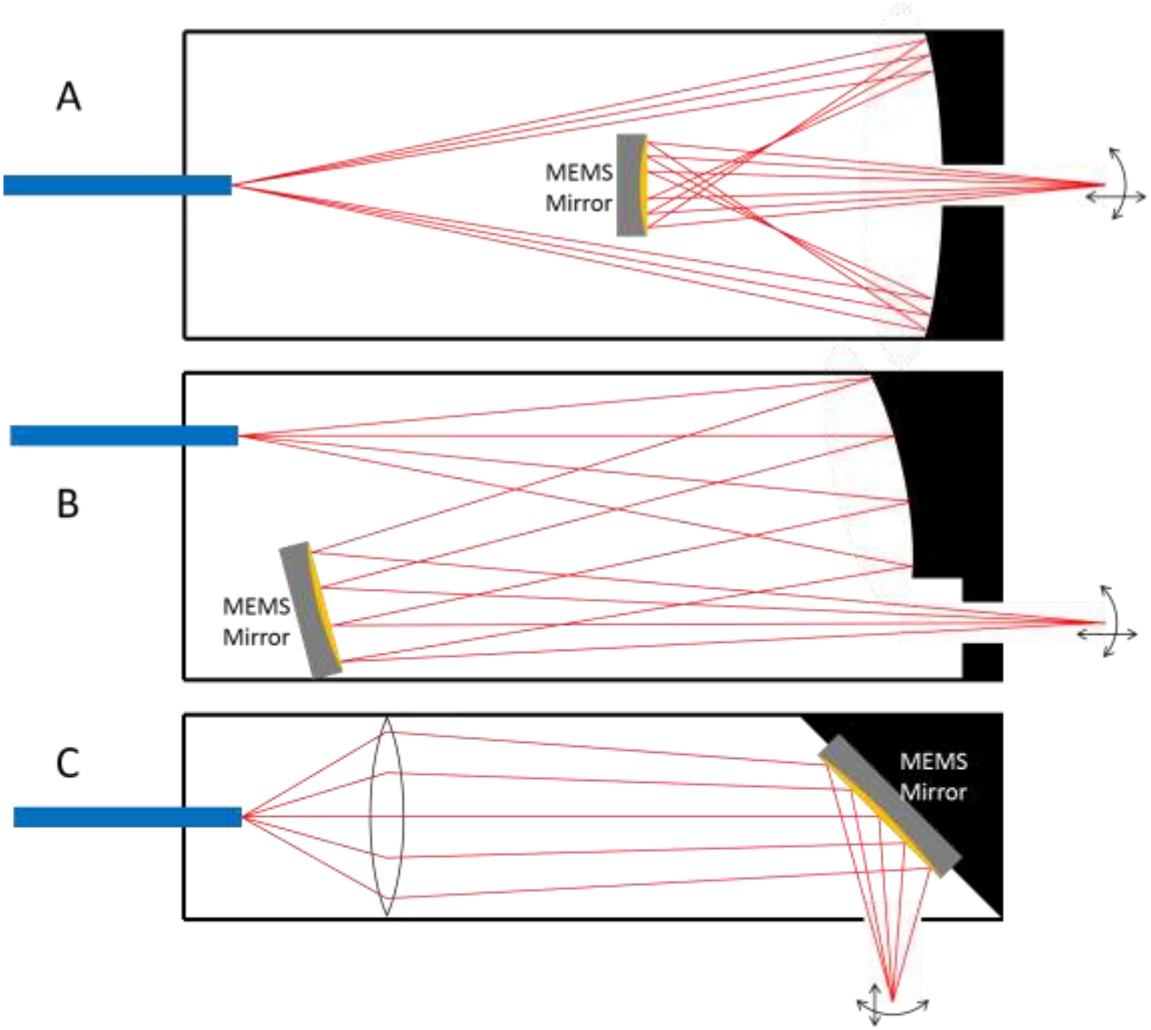

Fig 7.1: Schematics showing the design of three potential endoscopic imaging probes, two forward facing probes (a) and (b), and one side facing probe (c).

Both forward viewing probe designs use only reflective optical components. The side viewing probe, however, uses a lens to focus the light from the fiber, on to the MEMS mirror. Each of these designs has advantages and disadvantages for the optical system, and because of this the optimal packaging design is application dependent.

After packaging, this device will provide valuable functionality to an endoscopic OCT system, enabling 3-dimensional in-vivo imaging. Current CCD based endoscopes have the ability to produce high resolution 2-dimensional images. While allowing easy image acquisition and digital display, only the surface of the tissue is visible. The 3-dimensional MEMS scanner enables the imaging of sub-surface tissue, while also allowing focal control to improve the spatial resolution. Additionally, through the use of the same optical path, other optical microscopy techniques can be employed to further enhance the images generated.

References

[1] D. Huang, E. A. Swanson, C. P. Lin, J. S. Schuman, W. G. Stinson, W. Chang, M. R. Hee, T. Flotte, K. Gregory, C. A. Puliafito, and J. G. Fujimoto, “Optical Coherence Tomography,” vol. 245, no. 5035, pp. 1178–1181, 1991.

[2] M. C. Wu, O. Solgaard, and J. E. Ford, “Optical MEMS for Lightwave Communication,” *J. Light. Technol.*, vol. 24, no. 12, pp. 4433–4454, 2006.

[3] G. K. Fedder and L. R. Carley, “A low-noise low-offset capacitive sensing amplifier for a 50-/spl mu/g//spl radic/Hz monolithic CMOS MEMS accelerometer,” *IEEE J. Solid-State Circuits*, vol. 39, no. 5, pp. 722–730, May 2004.

[4] H. Xie and G. K. Fedder, “Fabrication, Characterization, and Analysis of a DRIE CMOS-MEMS Gyroscope,” *IEEE Sens. J.*, vol. 3, no. 5, pp. 622–631, 2003.

[5] B. Puers, E. Peeters, A. Van Den Bossche, and W. Sansen, “A capacitive pressure sensor with low impedance output and active suppression of parasitic effects,” *Sensors Actuators A Phys.*, vol. 21, no. 1–3, pp. 108–114, Feb. 1990.

[6] L. Hornbeck, “Active yoke hidden hinge digital micromirror device,” 1996.

[7] C. D. Lu, M. F. Kraus, B. Potsaid, J. J. Liu, W. Choi, V. Jayaraman, A. E. Cable, J. Hornegger, J. S. Duker, and J. G. Fujimoto, “Handheld ultrahigh speed swept source optical coherence tomography instrument using a MEMS scanning mirror.,” *Biomed. Opt. Express*, vol. 5, no. 1, pp. 293–311, Dec. 2013.

[8] J. Sun, S. Guo, L. Wu, L. Liu, S.-W. Choe, B. S. Sorg, and H. Xie, “3D In Vivo optical coherence tomography based on a low-voltage, large-scan-range 2D MEMS mirror,” *Opt. Express*, vol. 18, no. 12, pp. 12065–12075, 2010.

[9] A. D. Aguirre, P. R. Hertz, Y. Chen, J. G. Fujimoto, W. Piyawattanametha, L. Fan, and M. C. Wu, “Two-axis MEMS Scanning Catheter for Ultrahigh Resolution Three-dimensional and En Face Imaging.,” *Opt. Express*, vol. 15, no. 5, pp. 2445–2453, 2007.

[10] J. M. Edmonson, “History of the instruments for gastrointestinal endoscopy,” *Gastrointest. Endosc.*, vol. 37, pp. S27–S56, Mar. 1991.

[11] G. Berci and K. a. Forde, “History of endoscopy,” *Surg. Endosc.*, vol. 14, no. 1, pp. 5–15, Jan. 2000.

[12] C. M. Lee, C. J. Engelbrecht, T. D. Soper, F. Helmchen, and E. J. Seibel, “Scanning fiber endoscoppy with highly flexible, 1-mm catheterscopes for wide-field, full-color imaging,” *J. Biophotonics*, vol. 3, no. 5–6, pp. 385–407, 2010.

[13] L. An, P. Li, T. T. Shen, and R. Wang, “High speed spectral domain optical coherence tomography for retinal imaging at 500,000 A-lines per second.,” *Biomed. Opt. Express*, vol. 2, no. 10, pp. 2770–83, Oct. 2011.

[14] M. J. Cobb, X. Liu, and X. Li, “Continuous focus tracking for real-time optical coherence tomography.,” *Opt. Lett.*, vol. 30, no. 13, pp. 1680–1682, 2005.

[15] C. Fan, Y. Wang, and R. K. Wang, “Spectral domain polarization sensitive optical coherence tomography achieved by single camera detection,” *Opt. Express*, vol. 15, no. 13, pp. 7950–7961, 2007.

[16] J. G. Fujimoto, C. Pitris, S. a Boppart, and M. E. Brezinski, “Optical coherence tomography: an emerging technology for biomedical imaging and optical biopsy.,” *Neoplasia*, vol. 2, no. 1–2, pp. 9–25, 2000.

[17] W. Jung, D. T. McCormick, J. Zhang, L. Wang, N. C. Tien, and Z. Chen, “Three-dimensional endoscopic optical coherence tomography by use of a two-axis microelectromechanical scanning mirror,” *Appl. Phys. Lett.*, vol. 88, no. 16, p. 163901, 2006.

[18] K. H. Kim, B. H. Park, G. N. Maguluri, T. W. Lee, F. J. Rogomentich, M. G. Bancu, B. E. Bouma, J. F. de Boer, and J. J. Bernstein, “Two-axis magnetically-driven MEMS scanning catheter for endoscopic high-speed optical coherence tomography.,” *Opt. Express*, vol. 15, no. 26, pp. 18130–40, Dec. 2007.

[19] X. Liu, M. J. Cobb, Y. Chen, M. B. Kimmey, and X. Li, “Rapid-scanning forward-imaging miniature endoscope for real-time optical coherence tomography.,” *Opt. Lett.*, vol. 29, no. 15, pp. 1763–1765, 2004.

[20] T. Xie, H. Xie, G. K. Fedder, and Y. Pan, “Endoscopic optical coherence tomography with new MEMS mirror,” vol. 39, no. 21, pp. 9–10, 2003.

[21] Y. Pan, H. Xie, and G. K. Fedder, “Endoscopic optical coherence tomography based on a microelectromechanical mirror.,” *Opt. Lett.*, vol. 26, no. 24, pp. 1966–8, Dec. 2001.

[22] J. Sun and H. Xie, “MEMS-Based Endoscopic Optical Coherence Tomography,” *Int. J. Opt.*, vol. 2011, pp. 1–12, 2011.

[23] R. K. Wang, “In vivo full range complex Fourier domain optical coherence tomography,” *Appl. Phys. Lett.*, vol. 90, no. 5, p. 054103, 2007.

[24] B. Qi, P. A. Himmer, M. L. Gordon, V. X. D. Yang, D. L. Dickensheets, and A. I. Vitkin, “Dynamic focus control in high-speed optical coherence tomography based on a microelectromechanical mirror,” *Opt. Commun.*, vol. 232, no. 1–6, pp. 123–128, Mar. 2004.

[25] Y. Xu, J. Singh, C. S. Premachandran, a Khairyanto, K. W. S. Chen, N. Chen, C. J. R. Sheppard, and M. Olivo, “Design and development of a 3D scanning MEMS OCT probe using a novel SiOB package assembly,” *J. Micromechanics Microengineering*, vol. 18, no. 12, p. 125005, Dec. 2008.

[26] K. Aljasem, A. Werber, A. Seifert, and H. Zappe, “Fiber optic tunable probe for endoscopic optical coherence tomography,” *J. Opt. A Pure Appl. Opt.*, vol. 10, no. 4, p. 044012, Apr. 2008.

[27] Y. Shao and D. L. Dickensheets, “MOEMS 3-D scan mirror for single-point control of beam deflection and focus,” *J. Microlithogr. Microfabr. Microsystems*, vol. 4, no. 4, p. 041502, 2005.

[28] D. Hah, S. T.-Y. Huang, J.-C. Tsai, H. Toshiyoshi, and M. C. Wu, “Low-voltage, large-scan angle MEMS analog micromirror arrays with hidden vertical comb-drive actuators,” *J. Microelectromechanical Syst.*, vol. 13, no. 2, pp. 279–289, 2004.

[29] M. Strathman, Y. Liu, X. Li, and L. Y. Lin, “Dynamic focus-tracking MEMS scanning micromirror with low actuation voltages for endoscopic imaging,” *Opt. Express*, vol. 21, no. 20, pp. 23934–23941, 2013.

[30] K. E. Bean, “Anisotropic etching of silicon,” *IEEE Trans. Electron Devices*, no. 10, pp. 1185–1193, 1978.

[31] B. Puers and W. Sansen, “Compensation structures for convex corner micromachining in silicon,” *Sensors Actuators A Phys.*, vol. 23, no. 1–3, pp. 1036–1041, 1990.

[32] P. B. Chu, I. Brener, C. Pu, S. Lee, S. Member, J. I. Dadap, S. Park, K. Bergman, N. H. Bonadeo, T. Chau, M. Chou, R. A. Doran, R. Gibson, R. Harel, J. J. Johnson, C. D. Lee, D. R. Peale, B. Tang, D. T. K. Tong, M. Tsai, Q. Wu, W. Zhong, E. L. Goldstein, L. Y. Lin, and J. A. Walker, “Design and Nonlinear Servo Control of MEMS Mirrors and Their Performance in a Large Port-Count Optical Switch,” *J. Microelectromechanical Syst.*, vol. 14, no. 2, pp. 261–273, 2005.

[33] F. Laermer and A. Schilp, “United States Patent [19],” 1996.

[34] Y. Chen and X. Li, “Dispersion management up to the third order for real-time optical coherence tomography involving a phase or frequency modulator.,” *Opt. Express*, vol. 12, no. 24, pp. 5968–5978, 2004.

List of Abbreviations:

Abbreviation	Description
°C	Celsius, degrees (unit of temperature)
µm	Micrometer (unit of length)
AC	Alternating Current
A/D	Analog to Digital
AO	Acousto-Optic
Au	Gold
CCD	Charge Coupled Device
CF_4	Tetrafluoromethane
CHF_3	Trifluoromethane
Cr	Chrome
DC	Direct Current
DMD	Digital Micromirror Device
DRIE	Deep Reactive Ion Etching
EO	Electro-Optic
FWHM	Full Width Half Maximum
HF	Hydrofluoric acid
GI	Gastrointestinal
Hz	Hertz (unit of frequency)
KOH	Potassium hydroxide
kS/s	Kilo-Sample per Second (unit of sampling rate)
LPCVD	Low Pressure Chemical Vapor Deposition
MEMS	Micro-Electromechanical System

mm	Millimeter (unit of length)
n	Refractive index
NA	Numerical Aperature
nm	Nanometer (unit of length)
O2	Oxygen
OCT	Optical Coherence Tomography
PECVD	Plasma-Enhanced Chemical Vapor Deposition
RIE	Reactive Ion Etching
RSOD	Rapid Scanning Optical Delay line
SF_6	Sulfur Hexafluoride
Si	Silicon
SLD	Superluminescent diode
SMF	Single-Mode Fiber
SOI	Silicon On Insulator
TI	Texas Instruments
TV	Television
V	Volts (unit of voltage)

Appendix A: Matlab Code

Simulation calculations

```
% mirror tilt simulator
% all dimensions in micrometers


% Mirror Properties
WaferThickness = 250;
SiThickness = 30;
NitrideThickness = .5;
CrThickness = 0;
AuThickness = 0;
MirrorDiameter = 900;
MirrorRadius = MirrorDiameter/2;
MirrorElectrodeDiameter = 1070;
MirrorElectrodeRadius = MirrorElectrodeDiameter/2;
GimbalWidth = 90; % 40 or 60,   100 for OT
TrenchWidth = 20; % 50 or 70
TetherThickness = NitrideThickness;
TetherLength = TrenchWidth;
TetherWidth = 20; % 10, 15 or 20
PillarHeight = 000;
PillarSize = 1075;
PillarElectrodeGap = 30;
PillarElectrodeCenterCut = 200;
```

```
PillarCut = PillarElectrodeCenterCut+.5*PillarElectrodeGap;


V = zeros(26,701);

count = 1;


% Variable Parameters (comment all but 1)

for PillarCut = 15:20:515

% for MirrorElectrodeDiameter = 1200:100:1600 % lower voltage pull in as expected

%     MirrorElectrodeRadius = MirrorElectrodeDiameter/2;

% for WaferThickness = 50:10:300 % huge effect on pull in voltage

% for NitrideThickness = .5:.1:.9 % seemingly linear increase in actuation voltage

%     TetherThickness = NitrideThickness;

% for GimbalWidth = 60:20:140 % no effect on static actuation, will effect size and resonance

% for TrenchWidth = 40:10:80 % softens spring => fairly high effect on voltage

%     TetherLength = TrenchWidth;

% End Variable Parameters


%Mechanical Parameters

Gsini = 100; % approx. shear modulus of SiNi in GPa

G = 1e9*Gsini;

B = (1/3)*(1-(192/pi^5)*(TetherThickness/TetherWidth)*tanh((pi/2)*(TetherWidth/TetherThickness)));

% approx eqn B = 1/3-.21*(TetherThickness/TetherWidth)*(1-(TetherThickness^4/(12*TetherWidth^4)));



  E0 = 8.854e-18; % in F/um
```

```
  for DisplacementAngle = 0:.01:7 % degrees
    TiltAngle = DisplacementAngle*pi/180; % radians

   % Mechanical Torque
    Tm = 1e-18*TiltAngle*(2*G*TetherWidth*TetherThickness^3/TetherLength)*B;

   % Electrostatic torque
    AppliedVoltage = abs(MirrorVoltage-InnerElectrodeVoltage);
    Xradial = [1:MirrorElectrodeRadius];
    Displacement = tan(TiltAngle).*Xradial;
    ElectrodeSeparation = WaferThickness-SiThickness-PillarHeight-Displacement;
    BottomElectrodeArea = 2*((Xradial-.5)-sqrt(2*(PillarElectrodeGap/2)^2));
    for i = 1:round(sqrt(2*(PillarCut/2)^2))
      BottomElectrodeArea(i) = 0;
    end
    TopElectrodeArea = 2.*(Xradial-.5);
    for i = round(sqrt(2*(MirrorElectrodeRadius/2)^2)):MirrorElectrodeRadius
      TopElectrodeArea(i) = 2*MirrorElectrodeRadius*sin(acos((i-
.5)/MirrorElectrodeRadius));
    end
    ElectrodeOverlapArea = min(BottomElectrodeArea, TopElectrodeArea);

    % ElectrodeForce =
.5*E0*AppliedVoltage^2.*(ElectrodeOverlapArea./(ElectrodeSeparation.^2));
    % Te = sum(Xradial.*ElectrodeForce);
```

```
        TeV2 = sum(Xradial.*(.5*E0.*(ElectrodeOverlapArea./(ElectrodeSeparation.^2))));
        Va = sqrt(Tm/TeV2);

        if DisplacementAngle > 0
            if Va<V(count,round(DisplacementAngle*100))
                break
            else
                V(count,round(DisplacementAngle*100+1)) = Va;
            end
        else
            V(count,round(DisplacementAngle*100+1)) = Va;
        end
    end

    count = count+1;
end



angles = [0:.01:7];
figure('position',[100,100,800,600])
plot(V(1,:),angles,V(6,:),angles,V(11,:),angles,V(16,:),angles,V(21,:),angles,V(26,:),angles)
xlabel('Applied Voltage (V)','FontSize',18)
ylabel('Deflection Angle (degrees)','FontSize',18)
title('Deflection Angle vs. Applied Voltage','FontSize',24)
% legend(['080um'; '100um'; '120um'; '140um'; '160um'; '180um'; '200um'; '220um';
'240um'],'Location','EastOutside')
```

```
legend(['000um'; '100um'; '200um'; '300um'; '400um'; '500um'],'Location','EastOutside')


% figure(2)
% pillarcut = [0:20:500];
% plot(pillarcut,V(:,101),pillarcut,V(:,201),pillarcut,V(:,301),pillarcut,V(:,401),pillarcut,V(:,501),pillarcut,V(:,601),pillarcut,V(:,701))
electgap = [50:10:300];
% plot(electgap,V(:,101),electgap,V(:,201),electgap,V(:,301),electgap,V(:,401),electgap,V(:,501))


% xlabel('Pillar Electrode Cut (um)')
% ylabel('Applied Voltage')
% legend(['1deg';'2deg';'3deg';'4deg';'5deg';'6deg';'7deg'],'Location','EastOutside')
% ax = axis;
% axis([ax(1) ax(2) 0 ax(4)])
```

Calibration Code

```
function [VoltagesOut,InputData] = FullCal(dataFilename,voltages,dwell,ptsxout,ptsyout,extradata)
% dataFilename = complete path for log file from beam profiler
% voltages = column array of applied x and y voltages
% xdim, ydim = x and y dimensions of the input data
% dwell The dwell time at each point as defined in the Labview VI


%% Import data
```

```
fid = fopen(dataFilename);

testdata = textscan(fid, '%s');

fclose(fid);

testdata = testdata{1,1};

% start of data at point 80

% data titles

% Time   Centroid_H   Centroid_V   Beam Peak_H   Beam Peak_V   H_Width I   H_Width II
H_Width III   V_Width I   V_Width II   V_Width III   Power

nosamples = floor((length(testdata)-80)/12);

data = -99*ones(nosamples,12);

for i = 1:nosamples

    for j = 1:11

        data(i,j) = str2double(testdata(80+((i-1)*12)+(j-1)));

    end

end


for i = 1:length(data)

    if isnan(data(i,1));

        data = data(1:(i-1),:);

        break

    end

end


%% Remove extra points

cngthresh = 10000;

pts = length(voltages);
```

```
dify = diff(data(:,2));

difx = diff(data(:,3));

diffval = difx.^2 + dify.^2;

maxdiff = 0;

maxind = 0;

dn = 0;

for i = 1:200

    if diffval(i)>cngthresh

        dn = 1;

        if diffval(i)>maxdiff

            maxdiff = diffval(i);

            maxind = i;

        end

    elseif dn == 1

        break

    end

end


inds = getIndArray(data,maxind,dwell,pts+1);


sparceData = zeros(pts,2);

for i = 1:pts

    ind = inds(i);

    dind = inds(i+1)-ind;
```

```
    sparceData(i,1) = mean(data(floor(ind+.3*dind):ceil(ind+.7*dind),2));
    sparceData(i,2) = mean(data(floor(ind+.3*dind):ceil(ind+.7*dind),3));
end

InputData = [sparceData,voltages];

%% Data Alignment
[s,orig] = DefineAxes(sparceData);
xdir = [1,s]./abs(sqrt(1+s^2));
ydir = [-s,1]./abs(sqrt(1+s^2));

% Add ExtraData
data = [sparceData;extradata(:,1:2)];
voltages = [voltages;extradata(:,3:4)];

newdata = zeros(length(data),2);
for i = 1:length(data)
    newdata(i,1) = dot(xdir,[(data(i,1)-orig(1)),(data(i,2)-orig(2))]);
    newdata(i,2) = dot(ydir,[(data(i,1)-orig(1)),(data(i,2)-orig(2))]);
end
adata = newdata;

%% Plot data for confirmation
coords = DefineBox(adata);
x1 = coords(1,1);
```

```
x2 = coords(2,1);
y1 = coords(1,2);
y2 = coords(2,2);
ptsx = ptsxout;
ptsy = ptsyout;

%% Calibration
Ps = adata;
Vs = voltages;

tix = linspace(x1,x2,ptsx);
tiy = linspace(y1,y2,ptsy);

[Xi,Yi] = meshgrid(tix,tiy);
xVs = griddata(Ps(:,1),Ps(:,2),Vs(:,1),Xi,Yi,'cubic');
yVs = griddata(Ps(:,1),Ps(:,2),Vs(:,2),Xi,Yi,'cubic');

AppliedVoltages = cat(3,xVs,yVs);
vsout = AppliedVoltages;

%% Reshape voltages
VoltagesOutX = [];
VoltagesOutY = [];
for i = 1:ptsy;
   if mod(i,2) == 0
```

```
        VoltagesOutX = [VoltagesOutX;transpose(vsout(i,ptsx:-1:1,1))];
        VoltagesOutY = [VoltagesOutY;transpose(vsout(i,ptsx:-1:1,2))];
    else
        VoltagesOutX = [VoltagesOutX;transpose(vsout(i,:,1))];
        VoltagesOutY = [VoltagesOutY;transpose(vsout(i,:,2))];
    end
end
VoltagesOut = [VoltagesOutX,VoltagesOutY];
if max(isnan(VoltagesOut)) ~= 0
    VoltagesOut = nan
end
end



function [slp,orig] = DefineAxes(data)
PlotWindow2 = figure('Visible','off','Position',[200,300,540,400]);
a1 = axes('Units','pixels','position',[40,40,340,340]);
ChoosePoints = uicontrol('Style','PushButton','String','Define X-axis','Position',[400,285,120,30],'FontSize',12,'Callback',{@ChoosePoints_Callback});
Done = uicontrol('Style','PushButton','String','Done','Position',[400,85,120,30],'FontSize',12,'Callback',{@Done_Callback});
scatter(data(:,1),data(:,2));
set(PlotWindow2,'Visible','On');


function ChoosePoints_Callback(hObject, eventdata, handle)
```

```
    [x,y] = ginput(2);
    x1 = x(1);
    x2 = x(2);
    y1 = y(1);
    y2 = y(2);
    scatter(data(:,1),data(:,2));
    hold
    linx = line([x1,x2],[y1,y2]);
    hold
    orig = [x1,y1];
    slp = (y2-y1)/(x2-x1);
end
function Done_Callback(hObject, eventdata, handle)
    close(PlotWindow2);
end

disp('Hit any key to continue.')
pause
end



function coords = DefineBox(data)
PlotWindow2 = figure('Visible','off','Position',[200,300,540,400]);
a1 = axes('Units','pixels','position',[40,40,340,340]);
DefineBox = uicontrol('Style','PushButton','String','Define
Box','Position',[400,285,120,30],'FontSize',12,'Callback',{@DrawBox_Callback});
```

```
Done =
uicontrol('Style','PushButton','String','Done','Position',[400,85,120,30],'FontSize',12,'Callback',{
@Done_Callback});
scatter(data(:,1),data(:,2));
set(PlotWindow2,'Visible','On');


function DrawBox_Callback(hObject, eventdata, handle)
    [x,y] = ginput(2);
    x1 = min(x);
    x2 = max(x);
    y1 = min(y);
    y2 = max(y);
    scatter(data(:,1),data(:,2));
    hold
    linx1 = line([x1,x1],[y1,y2]);
    linx2 = line([x2,x2],[y1,y2]);
    liny1 = line([x1,x2],[y1,y1]);
    liny2 = line([x1,x2],[y2,y2]);
    hold
    coords = [x1,y1;x2,y2];
end
function Done_Callback(hObject, eventdata, handle)
    close(PlotWindow2);
end


disp('Hit any key to continue.')
```

```
pause
end



function indArray = getIndArray(data,strt,dt,pts)
% data is data from log file with headers removed
% strt index of first point of interest
% dt is dwell time
% pts is how many indexes are desired
t = data(strt,1);
cnt = 1;
indArray = zeros(1,pts);
indArray(1) = strt;
for i = (strt+1):length(data)
    if data(i,1)>=(t+dt*cnt)
        indArray(cnt+1) = i;
        cnt = cnt+1;
        if cnt > (pts-1)
            break
        end
    end
end
```